Phonon transport in disordered alloys: A Multiple-scattering approach

Aftab Alam *

Materials Modelling Laboratory, Department of Physics, Indian Institute of Technology Bombay, Mumbai 400076, India

(Received 25 April 2021; revised 24 July 2021; accepted 1 September 2021; published 15 September 2021)

I present a formalism to calculate the configuration-averaged lattice thermal conductivity for substitutional random alloys. The method is based on multiple-scattering approach which can capture the effect of disorder-induced configuration fluctuations on single-particle and two-particle phonon Green functions in random alloys. The randomness of the system is dealt within the augmented space theorem. This is combined with a generalized Feynman diagrammatic technique to extract various useful results in the form of mathematical expressions. I show the structure of all possible scattering diagrams up to the fourth order and subsequently illustrate how to obtain Dyson's equation from a resummation of the diagrammatic series. I also study how disorder scattering affects two-particle Green functions associated with thermal response. It was shown explicitly how the disorder scattering renormalizes both the phonon propagators as well as the heat currents. I derive the relation between these renormalized heat currents and the self-energy of the propagators. I have also studied a different class of scattering diagrams which are not related to the self-energy but rather to the vertex corrections. The configuration-averaging scheme is straightforward to apply to other relevant quantities such as joint density of states, thermal diffusivity, etc., for random alloys. The developed formalism is applied to a realistic $Au_{1-x}Fe_x$ binary alloy. The effect of disorder-induced corrections (as compared to the simple virtual crystal approximation) turns out to be appreciable in this alloy. The configuration-averaged lattice thermal conductivity for $Au_{50}Fe_{50}$ shows a quadratic behavior in low-temperature regime ($T \leqslant 30$ K), which increases smoothly to a T-independent saturated value at high T. Simulated thermal diffusivity $D(\nu)$ helps to numerically estimate the mobility edge (ν_c) which in turn evaluates the fraction of localized states. $D(\nu)$ is found to decrease smoothly (almost linearly) in the high-ν range, which when fitted to $(\nu_c - \nu)^\alpha$ gives the critical exponent (α) to be 1.018 for $Au_{50}Fe_{50}$ alloy. This agrees fairly well with the scaling and other theories of Andersen localization.

DOI: 10.1103/PhysRevB.104.104202

I. INTRODUCTION

Lattice thermal transport yields valuable information about the interactions of thermal excitations with composition fluctuations on the crystal lattice. Although the theory of lattice thermal conductivity for perfect crystals has been developed in some detail, the same is not true for substitutionally random alloys. In the problem of phonons, the presence of disorder not only arises from the impurity concentration, but also from the relative masses and size difference between the constituent atoms. It also depends on even more complex properties, namely, the difference in dynamical matrices of the constituent elements. For large mass and/or dynamical matrix differences, the effect of disorder can be quite unusual. A classic example is the random NiPt alloy, where both mass and dynamical matrix disorder dominates. The consequence of such a combination of disorder leads to the onset of split-band behavior in its phonon dispersion [1]. Note that, in NiPt alloy, the mass ($m_{\mathrm{Pt}} \sim 3m_{\mathrm{Ni}}$), size (12%), and the force constants ($\phi_{\mathrm{Pt\text{-}Pt}}$ is 55% larger than $\phi_{\mathrm{Ni\text{-}Ni}}$) of the constituent elements differ significantly, which gives rise to resonant modes [2]. Such split-band behavior is also observed experimentally [2].

Historically, the first proposal for the calculation of lattice thermal conductivity of disordered alloys was given by Leath [3] and Flicker and Leath [4] using the Kubo formula within the single-site coherent potential approximation (CPA). Similar technique is also used to calculate the electronic transport within CPA [3]. These are developed using multiple-scattering diagrams within the second-quantization Hamiltonian. It is well known that CPA is a single-site approximation and hence only capable of dealing with diagonal disorder (involving mass). It does not work for problems involving off-diagonal disorder such as those arising out of the force constants in the phonon problem [5]. This was shown explicitly for NiPt alloy where CPA gives a completely wrong phonon dispersion and lifetime [2]. The problem of phonon becomes even more complex due to the inherent presence of an environmental disorder arising out of the force constant sum rule, i.e., $\Phi_{RR} = -\sum_{R' \neq R} \Phi_{RR'}$. There are several proposals in the literature towards the generalization of CPA-type approach such as geometrically and linearly scaled off-diagonal disorder approximation [6], cluster coherent potential approximation (CCPA) [7], traveling cluster approximation (TCPA) [8], nonlocal CPA (NLCPA) [9], dynamical cluster approximation (DCA) [10], itinerant CPA (ICPA) [11], etc. A few of these later methods turn out to be reasonably successful in capturing the disorder-induced multiple-scattering effects. For example, ICPA is a self-consistent mean-field approach

* aftab@phy.iitb.ac.in

for the self-energy which relates the configuration-averaged Green function to the virtual crystal one. It is an approximation which maintains both the translational symmetry of the configuration average and its Herglotz analytic properties. In ICPA, contributions of configurations involving correlated fluctuations in more than one site to the self-energy are ignored. Another promising approach is typical medium DCA (a generalized version of DCA) [12] which systematically captures the effect of nonlocal spatial correlation and hence suitable for systems with off-diagonal disorder. Apart from these, there are also numerically exact approaches such as exact diagonalization [13], transfer matrix [14], and Kernel polynomial methods [15], which are often used to deal with systems acquiring off-diagonal disorder and strong localization effect. These methods are, however, mostly applicable to model systems of finite size. Although some of the above approximate methods were able to adequately capture the effects of both diagonal and off-diagonal disorders, their formalism was mostly restricted to the simulation of phonon dispersion, density of states, and phonon linewidths. A generalization of these approaches to the linear response level to simulate the thermal transport properties of random alloys is lacking. This is possibly due to a complex formulation.

In this communication, I present a detailed formalism to evaluate the effect of disorder scattering on the lattice thermal transport of random alloys. The method is based on a Kubo-Greenwood–type formula which relates the thermal conductivity to the heat (current-current) correlation function. To capture the randomness in the alloy, configuration averaging over several random atomic arrangements has been carried out using augmented space formalism (ASF), introduced by our group [16]. The ASF is a powerful technique which goes beyond the conventional mean-field approach and accurately capture the configuration fluctuations over a large local environment (including off-diagonal and other correlated disorders) [17–19]. Here, I shall combine a scattering diagram technique with the ASF for phonons [1] to get an effective heat current. This effective current captures the effect of various disorder scattering corrections, in addition to the standard averaged heat current. This disorder-induced correction will be shown to be directly related to either the disorder-scattering-induced self-energy matrix of the propagator or to the vertex correction. Similar scattering diagram approach has been used earlier by Leath [3], but within the framework of CPA. In this paper, I shall go beyond the single-site CPA and derive the contribution of these corrections for the most general case of phonon problem including diagonal (mass), off-diagonal, and environmental (dynamical matrix) disorder. The developed formalism is then applied on a real $Au_{1-x}Fe_x$ alloy within an *ab initio* framework. The application of the present method on a realistic material within a first-principles framework is a major advancement over other existing approaches.

II. FORMALISM

A. Effect of disorder on the single-particle Green function: The Dyson equation

The augmented space formalism (ASF) for carrying out configuration averaging of physical properties of disordered systems has been described in detail in several earlier papers [16,20,21]. I shall, for the sake of completeness, describe only those features which will be necessary for the implementation of our ideas in this communication.

Let $f(n_R)$ be a function of a binary random variable n_R, whose binary probability density is given by

$$Pr(n_R) \;=\; x_A\,\delta(n_R) \;+\; x_B\,\delta(n_R-1).$$

Such random variables are useful for describing substitutional binary alloys. These are the kind of disordered systems which I am interested in this communication. The ASF now prescribes that we write this probability density, which is a positive-definite integrable function, as the resolvent of an operator whose spectrum consists of the random values taken by it (in this case 0 and 1):

$$Pr(n_R) \;=\; -\frac{1}{\pi}\,\mathrm{Im}m\langle\uparrow_R|(n_R I - N_R)^{-1}|\uparrow_R\rangle. \qquad (1)$$

The *configuration space* of n_R is of rank two and spanned by the *states* $|0\rangle$ and $|1\rangle$. The operator N_R acts on this space. $|\uparrow_R\rangle = \sqrt{x_A}|0\rangle + \sqrt{x_B}|1\rangle$ is called the *reference state*. Its orthogonal counterpart is $|\downarrow_R\rangle = \sqrt{x_B}|0\rangle - \sqrt{x_A}|1\rangle$. The representation of N_R in this new basis is

$$N_R \;=\; \begin{pmatrix} x_A & \sqrt{x_A x_B} \\ \sqrt{x_A x_B} & x_B \end{pmatrix}.$$

The ASF now proceeds as follows:

$$\begin{aligned}
\langle\langle f(n_R)\rangle\rangle &= \int_{-\infty}^{\infty} f(n_R)Pr(n_R)dn_R \\
&= -\frac{1}{\pi}\mathrm{Im}\int_{-\infty}^{\infty} f(n_R)\langle\uparrow_R|(n_R I - N_R)^{-1}|\uparrow_R\rangle dn_R \\
&= -\frac{1}{\pi}\mathrm{Im}\sum_{\lambda=0,1}\sum_{\lambda'=0,1}\int_{-\infty}^{\infty} f(n_R) \\
&\quad\times\langle\uparrow_R|\lambda\rangle\langle\lambda|(n_R I - N_R)^{-1}|\lambda'\rangle\langle\lambda'|\uparrow_R\rangle dn_R \\
&= \sum_{\lambda=0,1}\langle\uparrow_R|\lambda\rangle f(\lambda)\langle\lambda|\uparrow_R\rangle \\
&= \langle\uparrow_R|\tilde{\mathbf{f}}|\uparrow_R\rangle. \qquad (2)
\end{aligned}$$

Here $\tilde{\mathbf{f}}$ is an operator built out of $f(n_R)$ by simply replacing the variable n_R by the associated operator N_R. The above expression shows that the average is obtained by taking the matrix element of this operator between the *reference state*$|\uparrow_R\rangle$. The full augmented space theorem is a generalization of this for functions of many independent random variables $\{n_R\}$.

The theory of phonons consists of solving a secular equation of the form

$$(\mathbf{M}w^2 - \mathbf{D})\,\mathbf{u}(R,w) = 0,$$

where $u_\alpha(R,w)$ is the Fourier transform of $u_\alpha(R,t)$, the displacement of an atom from its equilibrium position R on the lattice, in the direction α at time t. $\mathbf{M}$ is the *mass operator*, diagonal in real space, and $\mathbf{D}$ is the *dynamical matrix operator*

whose tight-binding representations are

$$\mathbf{M} = \sum_R m_R\, \delta_{\alpha\beta}\, P_R,$$

$$\mathbf{D} = \sum_R \left\{ -\sum_{R' \neq R} \Phi^{\alpha\beta}_{RR'} \right\} P_R + \sum_R \sum_{R' \neq R} \Phi^{\alpha\beta}_{RR'}\, T_{RR'}, \quad (3)$$

where the sum rule has been incorporated in the first term of the equation involving $\mathbf{D}$. Here P_R is the projection operator ($P_R = |R\rangle\langle R|$) and $T_{RR'}$ is the transfer operator ($T_{RR'} = |R\rangle\langle R'|$) in the real space $\mathcal{H}$ spanned by the tight-binding basis $\{|R\rangle\}$. R, R' specify the lattice sites and α, β the Cartesian directions. m_R is the mass of an atom occupying the position R and $\Phi^{\alpha\beta}_{RR'}$ is the force constant tensor.

I shall be interested in calculating the displacement-displacement Green matrix $\mathbf{G}(R, R', w^2)$:

$$\mathbf{G}(R, R', w^2) = \langle R| \left(\mathbf{M}w^2 - \mathbf{D}\right)^{-1} |R'\rangle.$$

Let us now consider a binary alloy A_xB_y consisting of two kinds of atoms A and B of masses m_A and m_B randomly occupying each lattice site. I wish to calculate the configuration-averaged Green matrix $\langle\langle \mathbf{G}(R, R', w^2)\rangle\rangle$. I shall use the augmented space formalism to do so indicating the main operational results here. For further details, I refer the reader to the above monograph, i.e., Ref. [21]. The first operation is to represent the random parts of the secular equation in terms of a random set of local variables $\{n_R\}$ which are 1 if the site R is occupied by an A atom and 0 if it is occupied by B.

In terms of these, the mass operator can be written as

$$\mathbf{M} = \sum_R [m_B + n_R\, (\delta m)]\delta_{\alpha\beta}\, P_R; \quad \delta m = m_A - m_B. \quad (4)$$

According to the augmented space theorem, in order to obtain the configuration average I simply replace the random variables n_R by the corresponding operators N_R associated with its probability density given by Eq. (1), and take the matrix element of the resulting operator between the *reference states*. For a full mathematical proof, the reader is referred to Ref. [21]:

$$n_R \longrightarrow N_R = x\, \tilde{I} + (y - x)\, p^{\downarrow}_R + \sqrt{xy}\, \mathcal{T}^{\uparrow\downarrow}_R.$$

Similarly, the random off-diagonal force constants $\Phi^{\alpha\beta}_{RR'}$ between the sites R and R' can be written as

$$\begin{aligned}\Phi^{\alpha\beta}_{RR'} &= \Phi^{\alpha\beta}_{AA} n_R n_{R'} + \Phi^{\alpha\beta}_{BB}(1 - n_R)(1 - n_{R'}) \\ &\quad + \Phi^{\alpha\beta}_{AB}[\, n_R(1 - n_{R'}) + n_{R'}(1 - n_R)\,] \\ &= \Phi^{\alpha\beta}_{BB} + \left(\Phi^{\alpha\beta}_{AA} + \Phi^{\alpha\beta}_{BB} - 2\Phi^{\alpha\beta}_{AB}\right) n_R n_{R'} \\ &\quad + \left(\Phi^{\alpha\beta}_{AB} - \Phi^{\alpha\beta}_{BB}\right)(n_R + n_{R'}). \end{aligned} \quad (5)$$

The augmented space theorem [16] yields the configuration-averaged Green function [20] as

$$\langle\langle \mathbf{G}(R, R', w^2)\rangle\rangle = \langle\{\emptyset\} \otimes R| \left(\mathbf{g}^{-1} - \widetilde{\mathbf{D}}_1\right)^{-1} |\{\emptyset\} \otimes R'\rangle, \quad (6)$$

where the virtual crystal approximated (VCA) Green matrix $\mathbf{g}$ is given by

$$\mathbf{g} = (\langle\langle \widetilde{\mathbf{M}}\rangle\rangle \omega^2 - \langle\langle \widetilde{\mathbf{D}}\rangle\rangle)^{-1},$$

where the mass operator $\widetilde{\mathbf{M}}$ and the dynamical matrix operator $\widetilde{\mathbf{D}}$, in the augmented space, has the following form:

$$\begin{aligned}\widetilde{\mathbf{M}} &= \mathbf{A}(\mathbf{m})\, \widetilde{I} \otimes I + \mathbf{B}(\mathbf{m}) \sum_R p^{\downarrow}_R \otimes P_R \\ &\quad + \mathbf{F}(\mathbf{m}) \sum_R \mathcal{T}^{\uparrow\downarrow}_R \otimes P_R \\ &= \langle\langle \widetilde{\mathbf{M}}\rangle\rangle + \widetilde{\mathbf{M}}', \end{aligned} \quad (7)$$

where

$$\begin{aligned}\mathbf{A}(\mathbf{X}) &= \langle\langle \mathbf{X}\rangle\rangle = (x\mathbf{X}_A + y\mathbf{X}_B), \\ \mathbf{B}(\mathbf{X}) &= (y - x)\, (\mathbf{X}_A - \mathbf{X}_B), \\ \mathbf{F}(\mathbf{X}) &= \sqrt{xy}\, (\mathbf{X}_A - \mathbf{X}_B), \end{aligned}$$

x, y being the concentration of the constituents A and B of the alloy A_xB_y. $p^{\downarrow}_R$ and $\mathcal{T}^{\uparrow\downarrow}_R$ are the projection and transfer operators in the configuration space describing the statistical behavior of the system

$$\begin{aligned}\langle\langle \widetilde{\mathbf{D}}\rangle\rangle &= -\sum_R \sum_{R' \neq R} \langle\langle \Phi_{RR'}\rangle\rangle \widetilde{I} \otimes P_R \\ &\quad + \sum_R \sum_{R' \neq R} \langle\langle \Phi_{RR'}\rangle\rangle \widetilde{I} \otimes T_{RR'}, \end{aligned} \quad (8)$$

where

$$\langle\langle \Phi_{RR'}\rangle\rangle = x^2\, \Phi_{AA} + y^2\, \Phi_{BB} + 2xy\, \Phi_{AB}.$$

Φ's in the right-hand side are the force constant tensor between different combinations of atoms. Also,

$$\begin{aligned}\widetilde{\mathbf{D}}_1 &= \sum_R \left\{ -\boldsymbol{\Upsilon}_R - \sum_{R' \neq R} \boldsymbol{\Psi}_{RR'} \right\} \otimes P_R \\ &\quad + \sum_R \sum_{R' \neq R} \boldsymbol{\Psi}_{RR'} \otimes T_{RR'} \end{aligned}$$

with

$$\boldsymbol{\Upsilon}_R = \mathbf{B}(\mathbf{m})\, \omega^2\, p^{\downarrow}_R + \mathbf{F}(\mathbf{m})\, \omega^2\, \mathcal{T}^{\uparrow\downarrow}_R,$$

$$\begin{aligned}\boldsymbol{\Psi}_{RR'} &= \mathbf{D}^{(1)}_{RR'}\, (p^{\downarrow}_R + p^{\downarrow}_{R'}) + \mathbf{D}^{(2)}_{RR'}\, (\mathcal{T}^{\uparrow\downarrow}_R + \mathcal{T}^{\uparrow\downarrow}_{R'}) \\ &\quad + \mathbf{D}^{(3)}_{RR'}\, p^{\downarrow}_R\, p^{\downarrow}_{R'} + \mathbf{D}^{(4)}_{RR'}\, (p^{\downarrow}_R\, \mathcal{T}^{\uparrow\downarrow}_{R'} \mathcal{T}^{\uparrow\downarrow}_R\, p^{\downarrow}_{R'}) \\ &\quad + \mathbf{D}^{(5)}_{RR'}\, \mathcal{T}^{\uparrow\downarrow}_R\, \mathcal{T}^{\uparrow\downarrow}_{R'}, \end{aligned} \quad (9)$$

where

$$\begin{aligned}&\mathbf{D}^{(1)} = (y - x)\, \Phi_{(1)}; \;\; \mathbf{D}^{(2)} = \sqrt{xy}\, \Phi_{(1)}, \\ &\mathbf{D}^{(3)} = (y - x)^2\, \Phi_{(2)}; \;\; \mathbf{D}^{(4)} = \sqrt{xy}\, (y - x)\, \Phi_{(2)}, \\ &\mathbf{D}^{(5)} = xy\, \Phi_{(2)} \end{aligned}$$

and

$$\begin{aligned}\Phi_{(1)} &= x\, \Phi_{AA} - y\, \Phi_{BB} + (y - x)\Phi_{AB}, \\ \Phi_{(2)} &= \Phi_{AA} + \Phi_{BB} - 2\Phi_{AB}. \end{aligned}$$

Physical interpretation of the vertices is transparent if I consider the $|\uparrow_R\rangle$ state to be the *ground state* or a state with no configuration fluctuations and $|\downarrow_R\rangle$ to be the state with one configuration fluctuation at the site R. The operator $p^{\downarrow}_R$ then

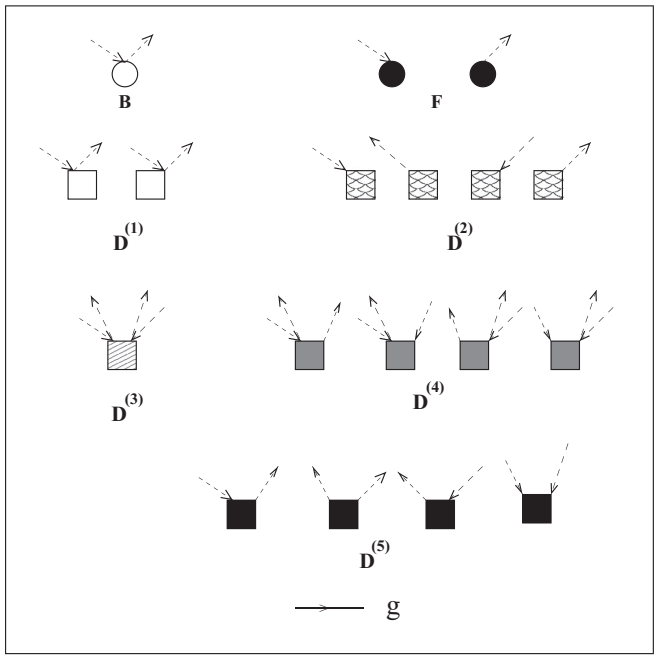

FIG. 1. The scattering vertices for the averaged Green function. These vertices correspond to various terms in Eqs. (7) and (8). The horizontal arrow line in the last row corresponds to the VCA green operator (**g**).

measures the number of fluctuations (0 or 1) and $\mathcal{T}_R^{\uparrow\downarrow}$ either creates or destroys a fluctuation at the site R.

Various terms of Eqs. (7) and (8) can then be represented by different vertices. These are shown in Fig. 1 corresponding to the scattering vertices **B**, **F** and $\mathbf{D}^{(1)}$-$\mathbf{D}^{(5)}$. The vertex **F** is diagonal in real space and causes a configuration fluctuation at a site due to disorder in the mass. Similarly, the vertex **B**, also diagonal in real space, counts the number of fluctuations at a given site. The remaining vertices labeled **D** are all off diagonal in real space. The vertex $\mathbf{D}^{(1)}$ counts the number of fluctuations at one or the other of the sites associated with the vertex. $\mathbf{D}^{(2)}$ causes a configuration fluctuation, again at one of the sites associated with the vertex. $\mathbf{D}^{(3)}$ counts the number of fluctuations at both the sites associated with the vertex. $\mathbf{D}^{(4)}$ counts the number of fluctuations at one site and causes a fluctuation at the other. Finally, $\mathbf{D}^{(5)}$ causes a fluctuation at both the sites associated with the vertex.

Equation (6) can also be expressed as

$$\langle\langle \mathbf{G}(R,R',w^2)\rangle\rangle = \langle\{\emptyset\}\otimes R|(\mathbf{g}+\mathbf{g}\,\widetilde{\mathbf{D}}_1\,\mathbf{g} + \mathbf{g}\,\widetilde{\mathbf{D}}_1\,\mathbf{g}\,\widetilde{\mathbf{D}}_1\,\mathbf{g}+\cdots)|\{\emptyset\}\otimes R'\rangle. \quad (10)$$

The first term in Eq. (10) gives

$$\langle\{\emptyset\}\otimes R|\,\mathbf{g}\,|\{\emptyset\}\otimes R'\rangle \;=\; \mathbf{g}(R,R',w^2).$$

Within the scattering diagram formalism, I shall associate a propagator represented by a horizontal arrow for each factor **g**. This is shown in the last row of Fig. 1. The second term in Eq. (10) yields zero since $\langle\{\emptyset\}\otimes R|\widetilde{\mathbf{D}}_1|\{\emptyset\}\otimes R'\rangle = 0$. The third term gives

$$\langle\{\emptyset\}\otimes R|\mathbf{g}\,\widetilde{\mathbf{D}}_1\,\mathbf{g}\,\widetilde{\mathbf{D}}_1\,\mathbf{g}|\{\emptyset\}\otimes R'\rangle = \sum_{S_1S_2}\sum_{S_3S_4}\sum_{\{\mathcal{C}\}}\sum_{\{\mathcal{C}'\}}\langle\{\emptyset\}\otimes R|\,\mathbf{g}\,|\{\emptyset\}\otimes S_1\rangle\langle\{\emptyset\}\otimes S_1|\,\widetilde{\mathbf{D}}_1\,|\{\mathcal{C}\}\otimes S''\rangle \times\langle\{\mathcal{C}\}\otimes S_2|\,\mathbf{g}\,|\{\mathcal{C}'\}\otimes S_3\rangle\langle\{\mathcal{C}'\}\otimes S_3|\,\widetilde{\mathbf{D}}_1\,|\{\emptyset\}\otimes S_4\rangle\,\langle\{\emptyset\}\otimes S_4|\,\mathbf{g}\,|\{\emptyset\}\otimes R'\rangle.$$

A little more algebra yields the following contribution:

$$\begin{aligned}\langle\{\emptyset\}\otimes R|\mathbf{g}\,\widetilde{\mathbf{D}}_1\,\mathbf{g}\,\widetilde{\mathbf{D}}_1\,\mathbf{g}|\{\emptyset\}\otimes R'\rangle = &\sum_{S_1S_2}\mathbf{g}(R,S_1,w^2)\,(\mathbf{F}w^2)\,\mathbf{g}(S_1,S_2,w^2)\,\delta(S_1-S_2)\,(\mathbf{F}w^2)\,\mathbf{g}(S_2,R',w^2)\\ &+\sum_{S_1}\sum_{S_3S_4}\mathbf{g}(R,S_1,w^2)\,(\mathbf{F}w^2)\,\mathbf{g}(S_1,S_3,w^2)\,\delta(S_1-S_3)\,\mathbf{D}^{(2)}_{S_3S_4}\,\mathbf{g}(S_4,R',w^2)\\ &+\sum_{S_1}\sum_{S_3S_4}\mathbf{g}(R,S_1,w^2)\,(\mathbf{F}w^2)\,\mathbf{g}(S_1,S_3,w^2)\,\delta(S_1-S_4)\,\mathbf{D}^{(2)}_{S_3S_4}\,\mathbf{g}(S_4,R',w^2)\\ &+\sum_{S_1}\sum_{S_2S_4}\mathbf{g}(R,S_1,w^2)\,\mathbf{D}^{(2)}_{S_1S_2}\,\mathbf{g}(S_2,S_4,w^2)\,\delta(S_1-S_4)\,(\mathbf{F}w^2)\,\mathbf{g}(S_4,R',w^2)\\ &+\sum_{S_1}\sum_{S_2S_4}\mathbf{g}(R,S_1,w^2)\,\mathbf{D}^{(2)}_{S_1S_2}\,\mathbf{g}(S_2,S_4,w^2)\,\delta(S_2-S_4)\,(\mathbf{F}w^2)\,\mathbf{g}(S_4,R',w^2)\\ &+\sum_{S_1S_2}\sum_{S_3S_4}\mathbf{g}(R,S_1,w^2)\,\mathbf{D}^{(2)}_{S_1S_2}\,\mathbf{g}(S_2,S_3,w^2)\,\delta(S_1-S_3)\,\mathbf{D}^{(2)}_{S_3S_4}\,\mathbf{g}(S_4,R',w^2)\\ &+\sum_{S_1S_2}\sum_{S_3S_4}\mathbf{g}(R,S_1,w^2)\,\mathbf{D}^{(2)}_{S_1S_2}\,\mathbf{g}(S_2,S_3,w^2)\delta(S_1-S_4)\,\mathbf{D}^{(2)}_{S_3S_4}\,\mathbf{g}(S_4,R',w^2)\\ &+\sum_{S_1S_2}\sum_{S_3S_4}\mathbf{g}(R,S_1,w^2)\,\mathbf{D}^{(2)}_{S_1S_2}\,\mathbf{g}(S_2,S_3,w^2)\,\delta(S_2-S_3)\,\mathbf{D}^{(2)}_{S_3S_4}\,\mathbf{g}(S_4,R',w^2)\end{aligned}$$

$$+\sum_{S_1S_2}\sum_{S_3S_4}\mathbf{g}(R,S_1,w^2)\,\mathbf{D}^{(2)}_{S_1S_2}\,\mathbf{g}(S_2,S_3,w^2)\,\delta(S_2-S_4)\,\mathbf{D}^{(2)}_{S_3S_4}\,\mathbf{g}(S_4,R',w^2)$$

$$+\sum_{S_1S_2}\sum_{S_3S_4}\mathbf{g}(R,S_1,w^2)\,\mathbf{D}^{(5)}_{S_1S_2}\,\mathbf{g}(S_2,S_3,w^2)\,\delta(S_2-S_4)\delta(S_1-S_3)\,\mathbf{D}^{(5)}_{S_3S_4}\,\mathbf{g}(S_4,R',w^2)$$

$$+\sum_{S_1S_2}\sum_{S_3S_4}\mathbf{g}(R,S_1,w^2)\,\mathbf{D}^{(5)}_{S_1S_2}\,\mathbf{g}(S_2,S_3,w^2)\,\delta(S_1-S_4)\delta(S_2-S_3)\,\mathbf{D}^{(5)}_{S_3S_4}\,\mathbf{g}(S_4,R',w^2). \quad (11)$$

Referring to the above equation, I shall now build up the scattering diagrams. I have already associated scattering vertices with the terms in $\widetilde{\mathbf{D}}_1$, as shown in Fig. 1. The dashed lines with arrow are associated with the delta function. A connected diagram to order "n" is built up by stringing together $(n+1)$ propagators associated with $\mathbf{g}$, connected by n vertices with all fluctuation lines combined in pairs. For $n=2$ there are 11 possible scattering diagrams, whose algebraic form is given in Eq. (11). These diagrams are shown in Fig. 2. For $n=3$, the possible kinds of scattering diagrams are shown in Fig. 3. Note that it involves terms with contribution from $\mathbf{B}$, $\mathbf{D}^{(1)}$, $\mathbf{D}^{(3)}$, and $\mathbf{D}^{(4)}$ as well. These scattering vertices can not sit either in the leftmost or in the rightmost positions because then one of the associated pseudo fermion Green function lines vanishes. In Figs. 3 A–3 F, each of the sections represents different distinct classes of diagrams. I call each section as the topologically distinct scattering diagrams. There exists three more sections in addition to these (i.e., Figs. 3 A–3 F) which are obtained simply by applying the reflection operators vertically to the diagrams in sections B, D, and E. Hence in total, there exist nine topologically distinct classes of scattering diagrams for $n=3$. For $n=4$, there are various classes of diagrams as shown in Fig. 4. In this figure, I have not shown the scattering diagrams with all sorts of combinations of fluctuation lines, but label the multiplicity within the parentheses for each diagram which actually gives the number of possible ways of combining the fluctuation lines for that particular diagram. For the diagram in the last column of Fig. 4 A, the middle decoration indicates a collection of all those diagrams lying in-between two vertices such that a single pseudofermion line goes out (from the left vertex) and a single pseudofermion line comes in (at the right vertex) for $n=4$. Similarly for the diagrams in the last column of Fig. 4 E, the middle decoration indicates a collection of all those diagrams lying in-between two vertices such that either (i) one pseudofermion line goes out (left vertex) and two pseudofermion line comes in (right vertex) or (ii) two pseudofermion lines go out (left vertex) and one pseudofermion line comes in (right vertex). For the diagrams in the last column of Fig. 4 I, the middle decoration

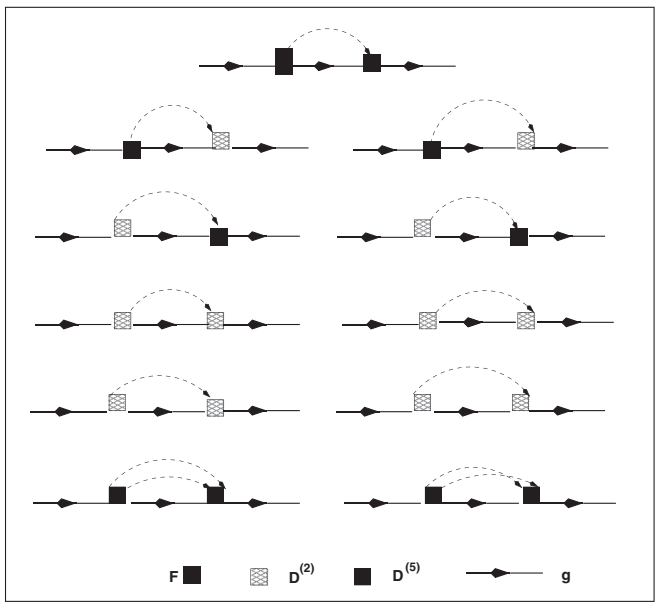

FIG. 2. The possible scattering diagrams for $n=2$.

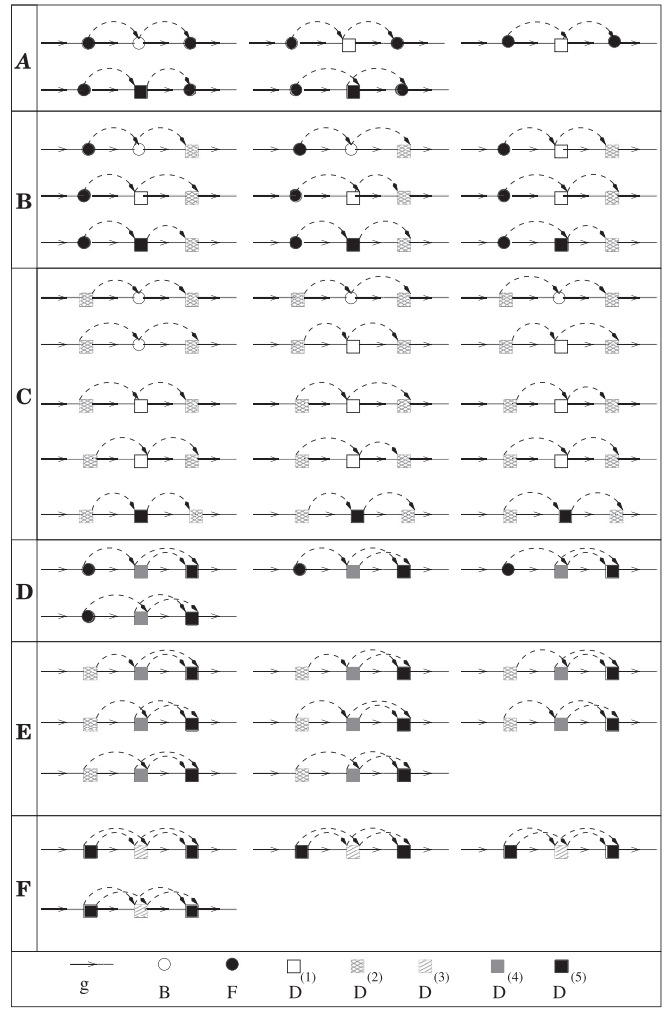

FIG. 3. The possible scattering diagrams for $n=3$.

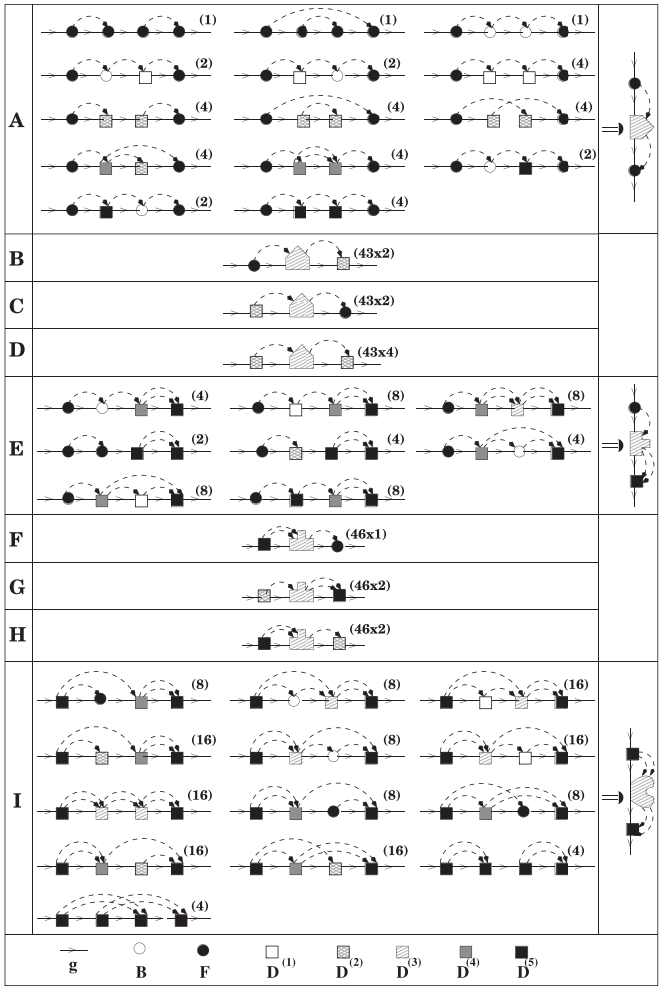

FIG. 4. The possible scattering diagrams for $n = 4$.

stands for a collection of all those diagrams lying in-between two vertices such that two pseudofermion lines go out (from the left vertex) and two pseudofermion lines come in (at the right vertex). Each of these diagrams in the last column are said to be the topologically distinct classes of diagrams. Hence, overall there exist nine topologically distinct classes of diagrams for $n = 4$ also.

Amongst the above sets of diagrams (for $n = 3$ and 4), there exist three basic subsets, namely,

(i) a set of separable diagrams, which are those that can be broken into two along a propagator line without also breaking a pseudofermion line;

(ii) a set of nonseparable, nonskeleton diagrams which can not be broken into two, but the VCA Green function in this diagram can be renormalized;

(iii) skeleton diagrams involving all the crossed and complicated structured diagrams.

If I club together the contribution of *all* the skeleton diagrams calling this the self-energy, and allow *all* phonon Green functions except the leftmost to be renormalized by the separable and nonseparable, nonskeleton diagrams, I get the Dyson equation

$$\langle\langle \mathbf{G} \rangle\rangle = \mathbf{g} + \mathbf{g}\ \mathbf{\Sigma} \langle\langle \mathbf{G} \rangle\rangle.$$

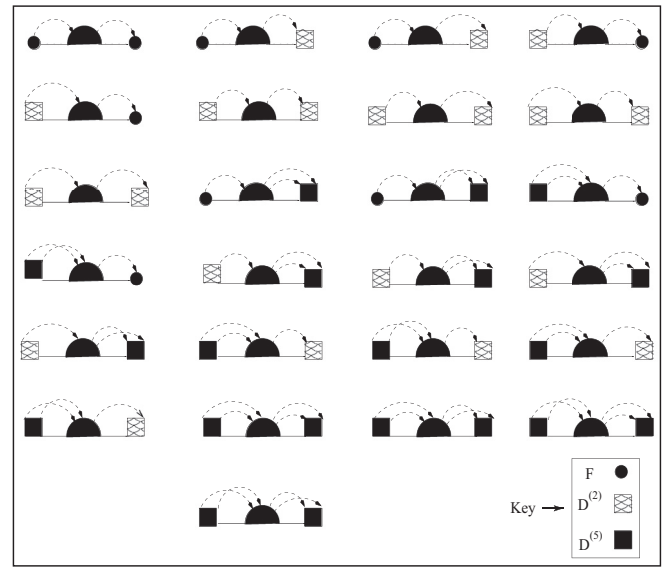

FIG. 5. Topological structure of the skeleton diagrams for the self-energy $\mathbf{\Sigma}$. The central dark semicircle represents all possible arrangements of scattering vertices to all orders.

For homogeneous disorder, it is already shown earlier by us that the translational symmetry remains intact in the full augmented space [22]. We can then take Fourier transform of the above equation to get

$$\langle\langle \mathbf{G}(\mathbf{q}, E) \rangle\rangle = \mathbf{g}(\mathbf{q}, E) + \mathbf{g}(\mathbf{q}, E)\ \mathbf{\Sigma}(\mathbf{q}, E)\ \langle\langle \mathbf{G}(\mathbf{q}, E) \rangle\rangle.$$

The diagrams for the self-energy are skeleton diagrams *all* of which have the structure as shown in Fig. 5. Each of these diagrams starts or ends with any one of either $\mathbf{F}$, $\mathbf{D}^{(2)}$, or $\mathbf{D}^{(5)}$ vertex. The central dark semicircle stands for all possible arrangements of scattering vertices to all orders.

B. Effect of disorder on two-particle Green functions: Lattice thermal conductivity

1. Configuration averaging of lattice thermal conductivity

The Kubo formula which relates the optical conductivity to a current-current correlation function is well established. The Hamiltonian contains a term $\sum_i \mathbf{j}_i \cdot \mathbf{A}(\underline{r}, t)$ which drives the electrical current. For thermal conductivity, I do not have a similar term in the Hamiltonian which drives a heat current. The derivation of a Kubo formula in this situation requires an additional statistical hypothesis which states that a system in steady state has a space-dependent *local* temperature $T(\underline{r}) = [\kappa_B \beta(\underline{r})]^{-1}$. The expression for the heat current has been discussed in great detail by Hardy [23] and Allen and Feldman [24]. The readers are referred to these papers for the details of calculation. The matrix element of the heat current in the basis of the eigenfunctions of the Hamiltonian is given by

$$\mathbf{S}^{\mu}_{\gamma\gamma'}(\mathbf{k}) = \frac{\hbar}{2}\ (\omega_{\mathbf{k}\gamma} + \omega_{\mathbf{k}\gamma'})\ \mathbf{v}^{\mu}_{\gamma\gamma'}(\mathbf{k}), \tag{12}$$

where the phonon group velocity $\mathbf{v}_{\gamma\gamma'}(\mathbf{k})$ is given by

$$\mathbf{v}_{\gamma\gamma'} = \frac{i}{2\sqrt{\omega_{\mathbf{k}\gamma}\omega_{\mathbf{k}\gamma'}}} \sum_{\mu}\sum_{\nu} \epsilon^{\mu}_{\gamma}(\mathbf{k})\, \epsilon^{\nu}_{\gamma'}(\mathbf{k}) \times \left(\sum_{\mathbf{R}_{ij}} \frac{\Phi^{\mu\nu}(\mathbf{R}_{ij})}{\sqrt{M_i M_j}}\right) \mathbf{R}_{ij}\, e^{i\mathbf{k}\cdot\mathbf{R}_{ij}} = \frac{1}{2\sqrt{\omega_{\mathbf{k}\gamma}\omega_{\mathbf{k}\gamma'}}} \sum_{\mu}\sum_{\nu} \epsilon^{\mu}_{\gamma}(\mathbf{k})\, \nabla_{\mathbf{k}} D^{\mu\nu}(\mathbf{k})\, \epsilon^{\nu}_{\gamma'}(\mathbf{k}), \quad (13)$$

where i, j label the atoms, γ, γ' label the various modes of vibrations, μ, ν label the Cartesian directions, $\omega_{\mathbf{k}\gamma}$, $\omega_{\mathbf{k}\gamma'}$ are the eigenfrequencies, $\epsilon^{\mu}_{\gamma}(\mathbf{k})$, $\epsilon^{\nu}_{\gamma'}(\mathbf{k})$ are the polarization vectors associated with the γth and γ'th mode of vibrations. $D^{\mu\nu}(\mathbf{k})$ is the Fourier transform of mass-scaled dynamical matrix.

I shall consider the case where the temperature gradient is uniform within the system. The linear heat current response is related to the temperature gradient field via a generalized susceptibility

$$\langle S^{\mu}(t)\rangle = -\sum_{\nu}\int_{-\infty}^{\infty} dt' \kappa^{\mu\nu}(t-t')\, \nabla^{\nu}\delta T(t).$$

The generalized susceptibility is the thermal conductivity in this case, given by

$$\kappa^{\mu\nu}(\tau) = \Theta(\tau)\, \frac{1}{T}\int_0^{\beta} d\lambda \langle S^{\mu}(-i\hbar\lambda), S^{\nu}(\tau)\rangle,$$

$\Theta(\tau)$ is the Heaviside step function, and

$$S(-i\hbar\lambda) \;=\; e^{\lambda H}\, S\, e^{-\lambda H},$$

the angle brackets on the right-hand side stand for thermal averaging over states in the absence of the temperature gradient. The above equation can be rewritten in the form of a Kubo-Greenwood expression

$$\kappa^{\mu\nu}(\omega, T) = \kappa_I^{\mu\nu}(\omega, T) \;+\; \kappa_{II}^{\mu\nu}(\omega, T),$$

$$\kappa_I^{\mu\nu}(\omega, T) = \frac{\pi}{T} \int \frac{d^3k}{8\pi^3} \sum_{\gamma,\gamma'\neq\gamma} \frac{\langle n_{\mathbf{k}\gamma'}\rangle - \langle n_{\mathbf{k}\gamma}\rangle}{\hbar(\omega_{\mathbf{k}\gamma} - \omega_{\mathbf{k}\gamma'})} \times \mathbf{S}^{\mu}_{\gamma\gamma'}(\mathbf{k})\mathbf{S}^{\nu}_{\gamma'\gamma}(\mathbf{k})\, \delta(\omega_{\mathbf{k}\gamma} - \omega_{\mathbf{k}\gamma'} - \omega), \quad (14)$$

$$\kappa_{II}^{\mu\nu}(\omega, T) = \frac{1}{\kappa_B T^2}\left[\left\{\int \frac{d^3k}{8\pi^3} \sum_{\gamma} \langle n_{\mathbf{k}\gamma}\rangle\, \mathbf{S}^{\mu}_{\gamma\gamma}(\mathbf{k})\right\} \times \left\{\int \frac{d^3k}{8\pi^3} \sum_{\gamma} \langle n_{\mathbf{k}\gamma}\rangle\, \mathbf{S}^{\nu}_{\gamma\gamma}(\mathbf{k})\right\} - \kappa_B T \int \frac{d^3k}{8\pi^3} \sum_{\gamma} \frac{\partial\langle n_{\mathbf{k}\gamma}\rangle}{\partial(\hbar\omega_{\mathbf{k}\gamma})}\, S^{\mu}_{\gamma\gamma}(\mathbf{k})\, S^{\nu}_{\gamma\gamma}(\mathbf{k})\right]\delta(\omega), \quad (15)$$

where $\langle n_{\mathbf{k}\gamma}\rangle = (e^{\beta\hbar\omega_{\mathbf{k}\gamma}} - 1)^{-1}$ is the equilibrium Bose-Einstein distribution function and T is the absolute temperature. For an isotropic response, Eq. (14), for interband transition, can be expressed as

$$\kappa_I(\omega, T) = \frac{\pi}{3T} \sum_{\mu} \int d\omega' \int \frac{d^3k}{8\pi^3} \sum_{\gamma,\gamma'} \widehat{\mathbf{S}}^{\mu}_{\gamma\gamma'}(\mathbf{k}, T)\widehat{\mathbf{S}}^{\mu}_{\gamma'\gamma}(\mathbf{k}, T) \times \delta(\omega' - \omega_{\mathbf{k}\gamma'})\delta(\omega' + \omega - \omega_{\mathbf{k}\gamma}), \quad (16)$$

where

$$\widehat{\mathbf{S}}^{\mu}_{\gamma\gamma'}(\mathbf{k}, T) \;=\; \sqrt{\left|\frac{\langle n_{\mathbf{k}\gamma'}\rangle - \langle n_{\mathbf{k}\gamma}\rangle}{\hbar(\omega_{\mathbf{k}\gamma} - \omega_{\mathbf{k}\gamma'})}\right|}\, \mathbf{S}^{\mu}_{\gamma\gamma'}(\mathbf{k}).$$

I can rewrite the above equation as

$$\kappa_I(\omega, T) = \frac{1}{3\pi T} \sum_{\mu} \int d\omega' \int \frac{d^3k}{8\pi^3} \mathrm{Tr}\big[\, \widehat{\mathbf{S}}^{\mu}(\mathbf{k}, T) \times \mathrm{Im}\{\mathbf{G}(\mathbf{k}, \omega')\}\, \widehat{\mathbf{S}}^{\mu}(\mathbf{k}, T)\, \mathrm{Im}\{\mathbf{G}(\mathbf{k}, \omega' + \omega)\}\big]. \quad (17)$$

The operator $\mathbf{G}(\omega)$ is the phonon Green operator $(M\omega^2\mathbf{I} - \mathbf{\Phi})^{-1}$. The trace is invariant in different representations. For crystalline systems, usually the Bloch basis $\{|\mathbf{k}, \gamma\rangle\}$ is used. For disordered systems, prior to configuration averaging, it is more convenient to use the basis $\{|\mathbf{k}, \alpha\rangle\}$, where $\mathbf{k}$ is the reciprocal vector and α represents the coordinate axes directions. I can transform from the mode basis to the coordinate basis by using the transformation matrices $\Upsilon_{\gamma\alpha}(\mathbf{k}) = \epsilon^{\alpha}_{\gamma}(\mathbf{k})$. For example,

$$\widehat{\mathbf{S}}^{\mu}_{\alpha\beta}(\mathbf{k}, T) \;=\; \Upsilon^{-T}_{\alpha\gamma}(\mathbf{k})\, \widehat{\mathbf{S}}^{\mu}_{\gamma\gamma'}(\mathbf{k}, T)\, \Upsilon^{-1}_{\gamma'\beta}(\mathbf{k}).$$

If I define

$$\kappa(z_1, z_2) = \int \frac{d^3k}{8\pi^3}\, \mathrm{Tr}\big[\, \widehat{\mathbf{S}}\, \mathbf{G}(\mathbf{k}, z_1)\, \widehat{\mathbf{S}}\, \mathbf{G}(\mathbf{k}, z_2)\big], \quad (18)$$

then Eq. (17) becomes

$$\kappa_I(\omega, T) = \frac{1}{12\pi T} \sum_{\mu} \int d\omega' \,[\kappa^{\mu\mu}(\omega'^{-}, \omega'^{+} + \omega) + \kappa^{\mu\mu}(\omega'^{+}, \omega'^{-} + \omega) - \kappa^{\mu\mu}(\omega'^{+}, \omega'^{+} + \omega) - \kappa^{\mu\mu}(\omega'^{-}, \omega'^{-} + \omega)], \quad (19)$$

where

$$f(\omega^{\pm}) = \lim_{\delta\to 0} f(\omega \pm i\delta).$$

I have also used the Herglotz analytic property of the Green operator

$$\mathbf{G}(\omega + i\delta) = \mathrm{Re}[\mathbf{G}(\omega)] - i\,\mathrm{sgn}(\delta)\, \mathrm{Im}[\mathbf{G}(\omega)].$$

For disordered materials, I am interested in obtaining the configuration-averaged response functions. This will require the configuration averaging of quantities like $\kappa(z_1, z_2)$. For disordered materials, Eq. (19) should be expressed as

$$\langle\langle\kappa_I(\omega, T)\rangle\rangle = \frac{1}{12\pi T} \sum_{\mu} \int d\omega' \,\langle\langle[\kappa^{\mu\mu}(\omega'^{-}, \omega'^{+} + \omega) + \kappa^{\mu\mu}(\omega'^{+}, \omega'^{-} + \omega) - \kappa^{\mu\mu}(\omega'^{+}, \omega'^{+} + \omega) - \kappa^{\mu\mu}(\omega'^{-}, \omega'^{-} + \omega)]\rangle\rangle, \quad (20)$$

Let us discuss the configuration averaging of the two-particle Green function of the kind $\kappa(z_1, z_2)$. The augmented space theorem immediately implies that

$$\langle\langle\kappa(z_1, z_2)\rangle\rangle = \mathrm{Tr}\big\langle\{\emptyset\}\big|\,[\widetilde{\mathbf{S}}\widetilde{\mathbf{G}}(z_1)\,\widetilde{\mathbf{S}}^{\dagger}\widetilde{\mathbf{G}}(z_2)]\,\big|\{\emptyset\}\big\rangle. \tag{21}$$

The first thing to note about Eq. (21) is that the right-hand side is an average of four random functions whose fluctuations are correlated. The average of the product then involves the product of the averages and other contributions which come from averages taken in pairs, triplets, and all four random functions.

Following a similar procedure as for a single-particle Green function, the operator $\widetilde{\mathbf{S}}$ in the augmented space takes the form

$$\begin{aligned}\widetilde{\mathbf{S}} = \sum_{R\alpha}\sum_{R'\alpha'}\big[&\langle\langle\widehat{\mathbf{S}}\rangle\rangle_{R\alpha,R'\alpha'}\widetilde{I} + \mathbf{S}^{(1)}_{R\alpha,R'\alpha'}(p^{\downarrow}_{R} + p^{\downarrow}_{R'})\\ &+\mathbf{S}^{(2)}_{R\alpha,R'\alpha'}(\mathcal{T}^{\uparrow\downarrow}_{R} + \mathcal{T}^{\uparrow\downarrow}_{R'}) + \mathbf{S}^{(3)}_{R\alpha,R'\alpha'}p^{\downarrow}_{R}\otimes p^{\downarrow}_{R'}\\ &+\mathbf{S}^{(4)}_{R\alpha,R'\alpha'}(p^{\downarrow}_{R}\otimes\mathcal{T}^{\uparrow\downarrow}_{R'} + p^{\downarrow}_{R'}\otimes\mathcal{T}^{\uparrow\downarrow}_{R})\\ &+\mathbf{S}^{(5)}_{R\alpha,R'\alpha'}\mathcal{T}^{\uparrow\downarrow}_{R}\otimes\mathcal{T}^{\uparrow\downarrow}_{R'}\big]\otimes T_{RR'},\end{aligned} \tag{22}$$

where

$$\begin{aligned}&\mathbf{S}^{(1)} = (y-x)\,\widehat{\mathbf{S}}^{(1)},\quad \mathbf{S}^{(2)} = \sqrt{xy}\,\widehat{\mathbf{S}}^{(1)},\\ &\mathbf{S}^{(3)} = (y-x)^2\,\widehat{\mathbf{S}}^{(2)},\quad \mathbf{S}^{(4)} = \sqrt{xy}\,(y-x)\,\widehat{\mathbf{S}}^{(2)},\\ &\mathbf{S}^{(5)} = xy\,\widehat{\mathbf{S}}^{(2)}\end{aligned}$$

and

$$\begin{aligned}\widehat{\mathbf{S}}^{(1)}_{R\alpha,R'\alpha'} &= x\big(\widehat{\mathbf{S}}^{AA}_{R\alpha,R'\alpha'} - \widehat{\mathbf{S}}^{AB}_{R\alpha,R'\alpha'}\big)\\ &\quad -y\big(\widehat{\mathbf{S}}^{BB}_{R\alpha,R'\alpha'} - \widehat{\mathbf{S}}^{BA}_{R\alpha,R'\alpha'}\big),\\ \widehat{\mathbf{S}}^{(2)}_{R\alpha,R'\alpha'} &= \widehat{\mathbf{S}}^{AA}_{R\alpha,R'\alpha'} + \widehat{\mathbf{S}}^{BB}_{R\alpha,R'\alpha'} - \widehat{\mathbf{S}}^{AB}_{R\alpha,R'\alpha'} - \widehat{\mathbf{S}}^{BA}_{R\alpha,R'\alpha'}.\end{aligned}$$

2. *Disorder-renormalized current*

I now start to set up the scattering diagrams for the thermal conductivity. A look at Eq. (22) shows us that the first term is the averaged VCA current. This term is absorbed in the unscattered part of the phonon Green function and leads to the zeroth-order approximation. Equation (22) looks very similar to Eq. (9) from the operator point of view. The only difference is that the former equation arises due to the disorder in heat currents while the latter equation due to the disorder in the dynamical matrix. Exactly as before, I can associate scattering vertices with the terms in $\widetilde{\mathbf{S}}$. Figure 6 shows 16 different scattering vertices arising out of the Eq. (22). Let us now discuss how the scattering diagrams are set up and then examine them. The rule for obtaining the diagrams for the correlation function $\langle\langle\kappa(z_1, z_2)\rangle\rangle$ is as follows: Take any two current diagrams from Fig. 6 and two propagators and join them end to end. Now join the configuration fluctuation lines (shown as dashed arrows) in all possible ways. The zeroth-order approximation for $\langle\langle\kappa(z_1, z_2)\rangle\rangle$ can be shown diagrammatically as in Fig. 7. The most dominant contribution comes from this particular diagram. Here the two current terms are the averaged current, and all configuration-fluctuation decorations renormalize only the two-phonon propagators. The bold propagators in this diagram are fully scattering renormalized propagators

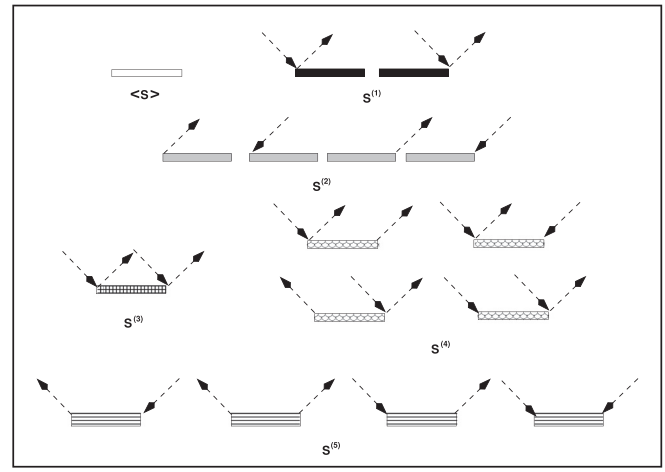

FIG. 6. The scattering vertices corresponding to the random heat-current terms]see Eq. (22)].

corresponding to the configuration-averaged Green function. The contribution of this term to the correlation function $\langle\langle\kappa(z_1, z_2)\rangle\rangle$ is

$$\int\frac{d^3k}{8\pi^3}\,\langle\langle\widehat{\mathbf{S}}(\mathbf{k})\rangle\rangle\langle\langle\mathbf{G}(\mathbf{k}, z_1)\rangle\rangle\langle\langle\widehat{\mathbf{S}}(\mathbf{k})\rangle\rangle\langle\langle\mathbf{G}(\mathbf{k}, z_2)\rangle\rangle. \tag{23}$$

The rest of the terms in Eq. (22) give rise to scattering. I shall now focus on the main correction terms to the expression in Eq. (23). These are the correction terms to the averaged current which, as I will show, are closely related to the self-energies. The first type of scattering diagrams are those in which no disorder propagator (shown as the dashed lines) joins either two-phonon propagators or two of the current lines directly. Figure 8 shows few such scattering diagrams. These sets of diagrams may be clubbed together and renormalized in a form which will consist of two fully renormalized phonon propagators connected at the two ends by a new form of the renormalized current. This new form of the renormalized current may be obtained in the following way.

Figure 8 clearly shows that these types of diagrams are made out of a left *renormalized* current diagram chosen out of any one of the diagrams from Figs. 9(a) and 9(b) and one right *renormalized* current diagram from any one of the diagram Figs. 9(c) and 9(d) connected by two *renormalized* propagators.

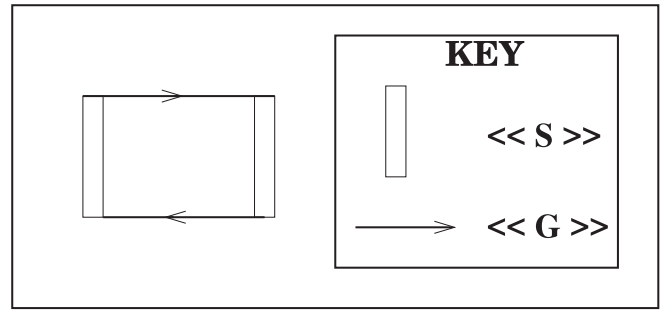

FIG. 7. The VCA or zeroth-order approximation for $\langle\langle\kappa(z_1, z_2)\rangle\rangle$.

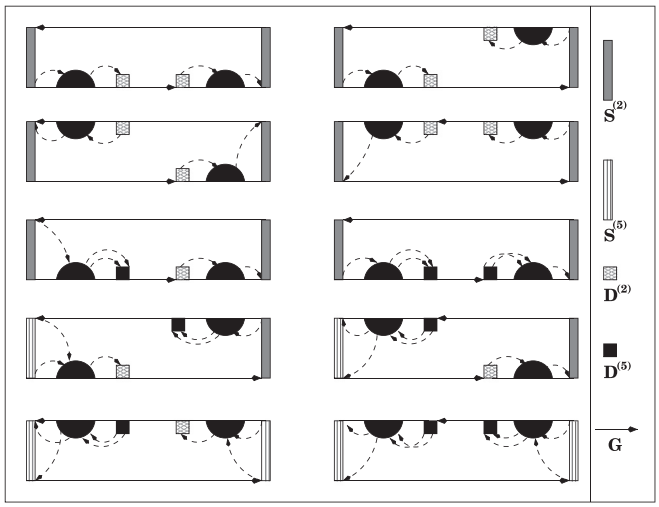

FIG. 8. Few examples of scattering diagrams where no disorder line joins the two-phonon propagators.

Let us now obtain expressions for the renormalized currents. A careful look at the self-energy diagrams (see Fig. 5) shows that all self-energy diagrams have the structure

$$\mathbf{\Sigma}(\mathbf{k}, z) = \Delta(\mathbf{k}, z)\ \ \mathbf{\Omega}(\mathbf{k}, z)\ \ \Delta(\mathbf{k}, z), \tag{24}$$

where $\mathbf{\Omega}(\mathbf{k}, z)$ is the Fourier transform of

$$\Omega_{RR'}(z) = \sum_{R_1 R_2} G_{RR_1}(z)\, P^{RR'}_{R_1 R_2}(z)\, G_{R_2 R'}(z) \tag{25}$$

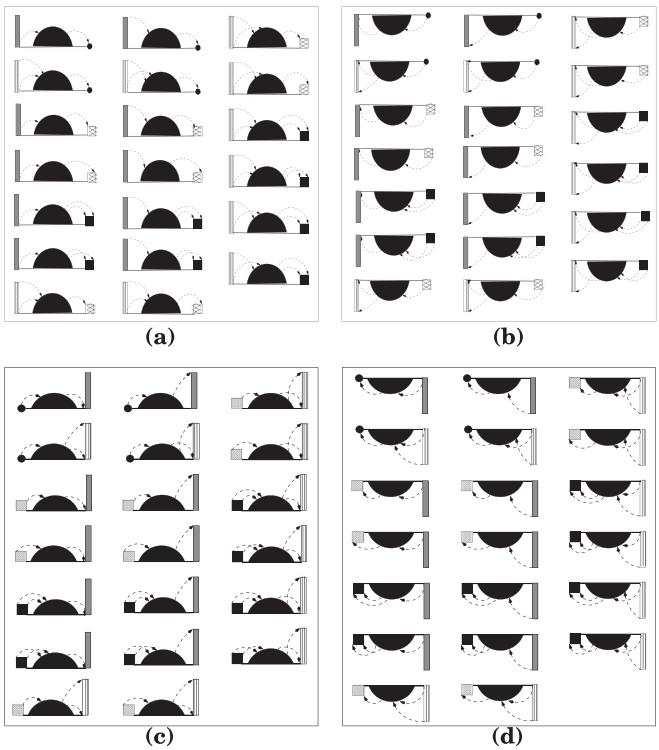

FIG. 9. Scattering diagrams contributing to effective heat current.

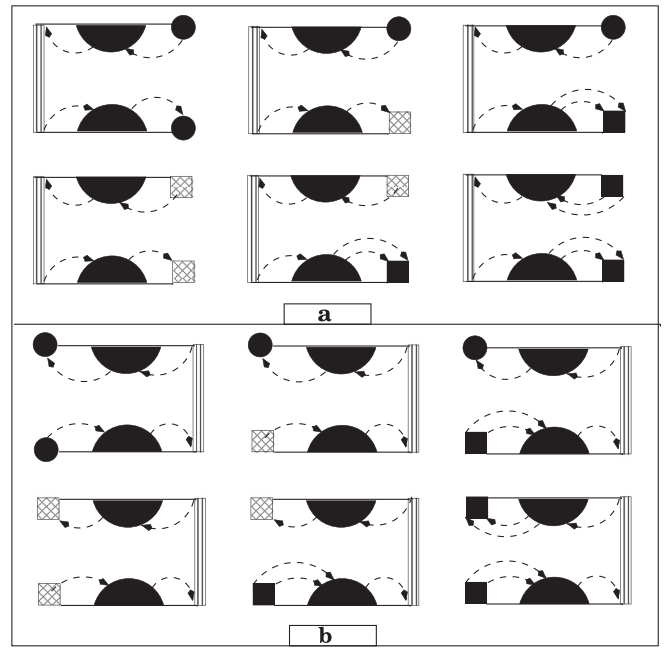

FIG. 10. The scattering diagrams associated with joint fluctuations of one current term and two propagators.

and

$$\Delta(\mathbf{k}, z) = \mathbf{F}\, z^2 + 2\, \mathbf{D}^{(2)}(\mathbf{k}) + 2\, \mathbf{D}^{(5)}(\mathbf{k}).$$

In the above equation, the quantity "P" stands for the central dark semicircle of Fig. 5 which represents all possible arrangements of scattering vertices to all orders.

If I compare the diagrams of Fig. 9(a) with the diagrams for the self-energy Fig. 5, I note that the only difference between the two is that the leftmost scattering vertex is replaced by a very similar heat-current term. In the diagrams of Fig. 9(a), the leftmost diagonal terms similar to the vertex $\mathbf{F}$ of Fig. 1 is of course missing. The contribution of such diagrams may be written in a mathematical form as

$$(2\, \mathbf{S}^{(2)}(\mathbf{k}) + 2\, \mathbf{S}^{(5)}(\mathbf{k}))\ \Omega(\mathbf{k}, z)\ \Delta(\mathbf{k}, z),$$

which may be expressed in terms of the self-energy "$\mathbf{\Sigma}$" by using Eq. (24) as

$$(2\, \mathbf{S}^{(2)}(\mathbf{k}) + 2\, \mathbf{S}^{(5)}(\mathbf{k}))\ [\Delta(\mathbf{k}, z_1)]^{-1}\ \mathbf{\Sigma}(\mathbf{k}, z_1).$$

The contribution of the diagrams in Fig. 9(b) is

$$\mathbf{\Sigma}(\mathbf{k}, z_2)\ [\Delta(\mathbf{k}, z_2)]^{-1} (2\, \mathbf{S}^{(2)}(\mathbf{k}) + 2\, \mathbf{S}^{(5)}(\mathbf{k})).$$

Similarly, the contribution of the diagrams in Figs. 9(c) and 9(d) are, respectively, given by

$$\mathbf{\Sigma}(\mathbf{k}, z_1)\ [\Delta(\mathbf{k}, z_1)]^{-1} (2\, \mathbf{S}^{(2)}(\mathbf{k}) + 2\, \mathbf{S}^{(5)}(\mathbf{k}))$$

and

$$(2\, \mathbf{S}^{(2)}(\mathbf{k}) + 2\, \mathbf{S}^{(5)}(\mathbf{k}))\ [\Delta(\mathbf{k}, z_2)]^{-1}\ \mathbf{\Sigma}(\mathbf{k}, z_2).$$

The next most dominant disorder corrections come from a group of diagrams which describe joint fluctuation of one current and two propagators. A few such diagrams are shown in Fig. 10.

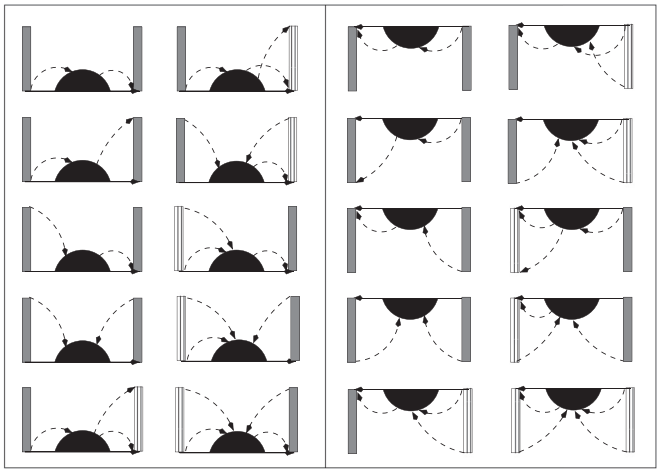

FIG. 11. The scattering diagrams associated with joint fluctuations of two current terms and one propagator.

The contributions of these diagrams [Figs. 10(a) and 10(b)] can also be expressed in terms of the self-energy as

$$\text{(a)}\ \ \boldsymbol{\Sigma}(\mathbf{k}, z_2)\,[\Delta(\mathbf{k}, z_2)]^{-1}\,\mathbf{S}^{(5)}(\mathbf{k})[\Delta(\mathbf{k}, z_1)]^{-1}\,\boldsymbol{\Sigma}(\mathbf{k}, z_1),$$

$$\text{(b)}\ \ \boldsymbol{\Sigma}(\mathbf{k}, z_1)\,[\Delta(\mathbf{k}, z_1)]^{-1}\,\mathbf{S}^{(5)}(\mathbf{k})[\Delta(\mathbf{k}, z_2)]^{-1}\,\boldsymbol{\Sigma}(\mathbf{k}, z_2).$$

If I now gather all the contributions from these diagrams [from Figs. 9(a)–9(d) and 10(a) and 10(b)], I can define a renormalized current term as follows:

$$\mathbf{S}_{\text{eff}}(\mathbf{k}, z_1, z_2) = \langle\langle\widehat{\mathbf{S}}(\mathbf{k})\rangle\rangle + \Delta\mathbf{S}_1(\mathbf{k}, z_1, z_2) + \Delta\mathbf{S}_2(\mathbf{k}, z_1, z_2), \tag{26}$$

where

$$\begin{aligned}\Delta\mathbf{S}_1(\mathbf{k}, z_1, z_2) &= 2[\mathbf{S}^{(2)}(\mathbf{k}) + \mathbf{S}^{(5)}(\mathbf{k})][\Delta(\mathbf{k}, z_1)]^{-1}\boldsymbol{\Sigma}(\mathbf{k}, z_1)\\ &\quad + \boldsymbol{\Sigma}(\mathbf{k}, z_2)[\Delta(\mathbf{k}, z_2)]^{-1}2[\mathbf{S}^{(2)}(\mathbf{k}) + \mathbf{S}^{(5)}(\mathbf{k})],\\ \Delta\mathbf{S}_2(\mathbf{k}, z_1, z_2) &= \boldsymbol{\Sigma}(\mathbf{k}, z_2)[\Delta(\mathbf{k}, z_2)]^{-1}\mathbf{S}^{(5)}(\mathbf{k})[\Delta(\mathbf{k}, z_1)]^{-1}\\ &\quad \times\boldsymbol{\Sigma}(\mathbf{k}, z_1).\end{aligned}$$

The contribution of these disorder-renormalized currents and propagators to the correlation function is

$$\begin{aligned}\langle\langle\kappa_{(1)}(z_1, z_2)\rangle\rangle = \int \frac{d^3k}{8\pi^3}\text{Tr}[&\mathbf{S}_{\text{eff}}(\mathbf{k}, z_1, z_2)\langle\langle\mathbf{G}(\mathbf{k}, z_1)\rangle\rangle\\ &\times\mathbf{S}^{\dagger}_{\text{eff}}(\mathbf{k}, z_1, z_2)\langle\langle\mathbf{G}(\mathbf{k}, z_2)\rangle\rangle].\end{aligned} \tag{27}$$

I shall now discuss the disorder correction terms which involve joint fluctuations between the two current terms and one propagator. Few such diagrams are shown in Fig. 11. A close inspection of these diagrams shows that these are also related to the self-energy diagrams with vertices at both ends replaced by currents. The corrections due to these terms can therefore be related to the self-energy as before.

The contribution of these diagrams to the correlation function is given by

$$\begin{aligned}\langle\langle\kappa_{(2)}(z_1, z_2)\rangle\rangle = 4\int \frac{d^3k}{8\pi^3}\text{Tr}[&\Delta\mathbf{S}_3(\mathbf{k}, z_1)\langle\langle\mathbf{G}(\mathbf{k}, z_2)\rangle\rangle\\ &+ \Delta\mathbf{S}_4(\mathbf{k}, z_2)\langle\langle\mathbf{G}(\mathbf{k}, z_1)\rangle\rangle],\end{aligned} \tag{28}$$

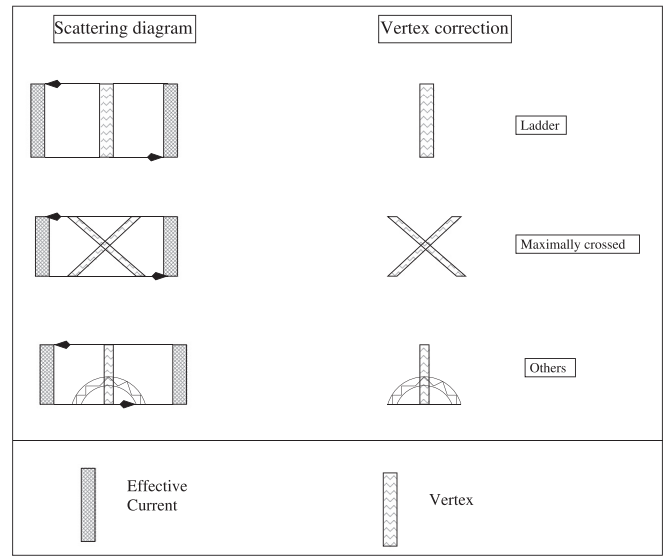

FIG. 12. Various scattering diagrams, such as ladder diagram, maximally crossed diagram, etc., leading to vertex correction.

where

$$\begin{aligned}\Delta\mathbf{S}_3(\mathbf{k}, z_1) &= (\mathbf{S}^{(2)}(\mathbf{k}) + \mathbf{S}^{(5)}(\mathbf{k}))[\Delta(\mathbf{k}, z_1)]^{-1}\\ &\quad\times\boldsymbol{\Sigma}(\mathbf{k}, z_1)[\Delta(\mathbf{k}, z_1)]^{-1}(\mathbf{S}^{(2)}(\mathbf{k}) + \mathbf{S}^{(5)}(\mathbf{k}))^{\dagger},\\ \Delta\mathbf{S}_4(\mathbf{k}, z_2) &= (\mathbf{S}^{(2)}(\mathbf{k}) + \mathbf{S}^{(5)}(\mathbf{k}))[\Delta(\mathbf{k}, z_2)]^{-1}\\ &\quad\times\boldsymbol{\Sigma}(\mathbf{k}, z_2)[\Delta(\mathbf{k}, z_2)]^{-1}(\mathbf{S}^{(2)}(\mathbf{k}) + \mathbf{S}^{(5)}(\mathbf{k}))^{\dagger}.\end{aligned}$$

In our earlier paper [25] on a similar problem, I have argued that these are the dominant disorder corrections to the average current. Intuitively, I also expect the same to be true in the present case as well. It is important to note that these corrections can be obtained from the self-energy and is therefore computationally feasible in the case of realistic alloys, once I have a feasible method for obtaining the self-energy.

There are other scattering diagrams which are not related to the self-energy but rather to the vertex corrections. In these diagrams, a disorder line connects both the phonon propagators directly. These are the diagrams which are possibly responsible for the weak localization. For the sake of completeness, I shall indicate in detail how to obtain them within a ladder diagram approximation in the next subsection.

3. Vertex correction

The vertex corrections are basically those scattering diagrams in which disorder lines connect both the propagators directly. I have not yet incorporated these kinds of diagrams in the disorder renormalization. These diagrams arise due to the correlated propagation. The diagrams leading to the vertex corrections may be of different kinds, e.g., ladder diagrams, maximally crossed diagrams, etc. The ladder diagrams are those which are built out of repeated vertices, as shown on the first row of Fig. 12. These kinds of diagrams can be summed up to all orders. This is the disorder scattering version of the *random-phase approximation* (RPA) for the phonon-phonon scattering. The maximally crossed diagrams are those diagrams in which the ladder inserts between the crossed

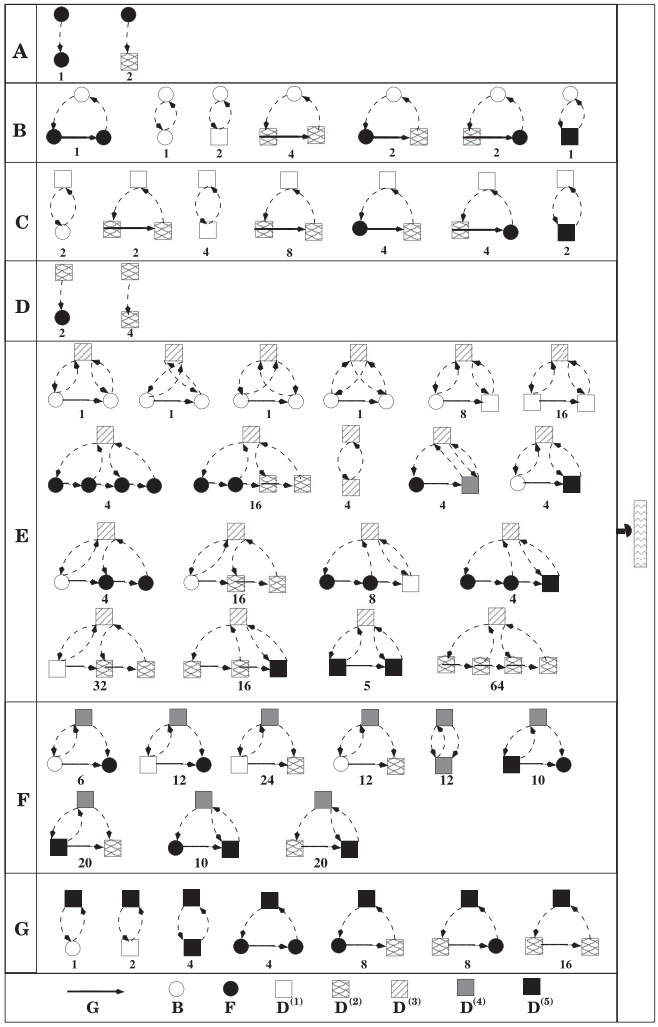

FIG. 13. The ladder scattering diagrams for the vertex correction.

vertices. These types of diagrams are shown in the second row of Fig. 12. Here I shall consider the ladder diagrams in detail and show how to obtain the contribution of these diagrams in terms of mathematical expression. I then sum these ladder diagrams to all orders. The possible scattering diagrams for the ladder kind of vertex correction involving the vertices **B**, **F**, $\mathbf{D}^{(1)}$ to $\mathbf{D}^{(5)}$ are shown in Fig. 13.

The contribution of seven categories (A–G), shown in Fig. 13, of the ladder scattering diagrams in terms of mathematical expressions $[(W^{\gamma\delta}_{\alpha\beta})_i,\ i = \text{A–G}]$ are presented in the Appendix. Considering the above seven categories, the sum of all possible scattering diagrams contributing to the four-legged vertex (shown in the extreme right column of Fig. 13) will be given by

$$W^{\gamma\delta}_{\alpha\beta} = \sum_{i=A}^{G} \left(W^{\gamma\delta}_{\alpha\beta}\right)_i.$$

Here I shall sum the ladder diagrams to all orders. The contribution of a single ladder diagram to the correlation function, as shown in the first row of Fig. 14, can be mathematically

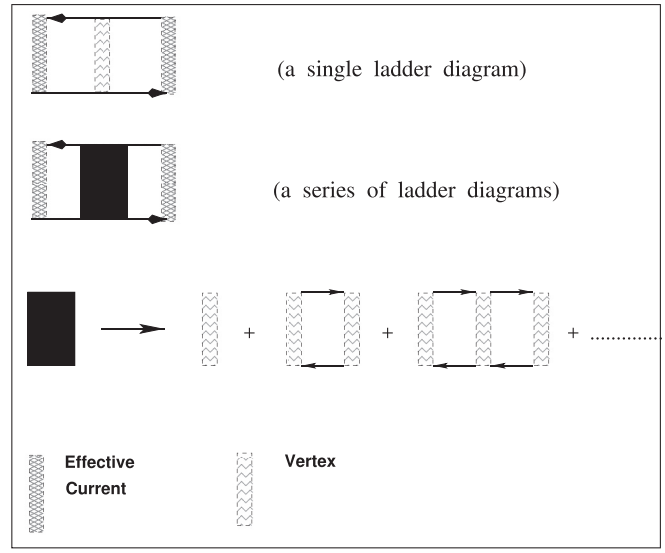

FIG. 14. The structure of infinite series of ladder diagrams contributing to the correlation function $\langle\langle \kappa(z_1, z_2)\rangle\rangle$.

expressed as

$$\sum_{R_1R_2}\sum_{R_3R_4}\sum_{R_5}\sum_{\alpha_1\alpha_2}\sum_{\alpha_3\alpha_4}\sum_{\alpha_5\alpha_6} S^{\text{eff}}_{R_5\alpha_6,R_1\alpha_1}\, G_{R_1\alpha_1,R_2\alpha_2}(z_1) \times W^{\alpha_5\alpha_5}_{\alpha_2\alpha_2}\, G_{R_2\alpha_2,R_3\alpha_3}(z_1)\left(S^{\text{eff}}_{R_3\alpha_3,R_4\alpha_4}\right)^{\dagger} \times G_{R_4\alpha_4,R_2\alpha_5}(z_2)\, G_{R_2\alpha_5,R_5\alpha_6}(z_2). \tag{29}$$

If I apply the homogeneity in full augmented space, it will imply that the above expression is independent of "R" which allows us to take the Fourier transform leading to the following expression:

$$\left[\int_{\text{BZ}} \frac{d^3k}{8\pi^3}\, \mathbf{G}(\mathbf{k}, z_2)\mathbf{S}^{\text{eff}}(\mathbf{k}, z_1, z_2)\mathbf{G}(\mathbf{k}, z_1)\right]\mathbf{W} \times \left[\int_{\text{BZ}} \frac{d^3k'}{8\pi^3}\, \mathbf{G}(\mathbf{k}', z_1)(\mathbf{S}^{\text{eff}}(\mathbf{k}', z_1, z_2))^{\dagger}\mathbf{G}(\mathbf{k}', z_2)\right] = \mathbf{\Gamma}(z_1, z_2)\, \mathbf{W}\, \widehat{\mathbf{\Gamma}}(z_1, z_2),$$

where I have defined

$$\mathbf{\Gamma}(z_1, z_2) = \int_{\text{BZ}} \frac{d^3k}{8\pi^3}\mathbf{G}(\mathbf{k}, z_2)\mathbf{S}^{\text{eff}}(\mathbf{k}, z_1, z_2)\mathbf{G}(\mathbf{k}, z_1),$$

$$\widehat{\mathbf{\Gamma}}(z_1, z_2) = \int_{\text{BZ}} \frac{d^3k'}{8\pi^3}\mathbf{G}(\mathbf{k}', z_1)(\mathbf{S}^{\text{eff}}(\mathbf{k}', z_1, z_2))^{\dagger}\mathbf{G}(\mathbf{k}', z_2).$$

Let us now look at the contribution of the infinite series of ladder diagrams (shown in the third row of Fig. 14) to the correlation function. Each one of them has the same structure as Eq. (29). I can then sum up the series as follows.

Let us define

$$\mathbf{\Theta}^{\gamma\delta}_{\alpha\beta}(z_1, z_2) = \int_{\text{BZ}} \frac{d^3k}{8\pi^3}\, G_{\alpha\beta}(\mathbf{k}, z_1)\, G_{\gamma\delta}(\mathbf{k}, z_2).$$

Then,

$$\mathbf{\Lambda}(z_1, z_2) = \mathbf{W} + \mathbf{W}\mathbf{\Theta}\mathbf{W} + \mathbf{W}\mathbf{\Theta}\mathbf{W}\mathbf{\Theta}\mathbf{W} + \cdots = \mathbf{W}(z_1, z_2)(\mathbf{I} - \mathbf{\Theta}(z_1, z_2)\mathbf{W}(z_1, z_2))^{-1}.$$

Thus, the contribution of the infinite series of ladder diagram vertex corrections to the correlation function may be expressed as

$$\langle\langle \Delta\kappa(z_1, z_2)^{\text{ladder}}\rangle\rangle = \sum_{\alpha\beta}\sum_{\gamma\delta} \mathbf{\Gamma}^{\alpha}_{\beta}(z_1, z_2)\mathbf{\Lambda}^{\alpha\nu}_{\beta\delta}(z_1, z_2) \times \widehat{\mathbf{\Gamma}}^{\nu}_{\delta}(z_1, z_2). \quad (30)$$

Including all types of disorder corrections [as derived in Eqs. (21), (28), and (30)], the configuration average of the correlation function will have the following form:

$$\langle\langle \kappa(z_1, z_2)\rangle\rangle = \langle\langle \kappa_{(1)}(z_1, z_2)\rangle\rangle + \langle\langle \kappa_{(2)}(z_1, z_2)\rangle\rangle + \langle\langle \Delta\kappa(z_1, z_2)^{\text{ladder}}\rangle\rangle. \quad (31)$$

It can be shown that the transition rate $\beta(\nu, T)$ (related to the heat-current operator) is strongly dependent on both initial and final energies throughout the phonon spectrum by simply calculating the configuration-averaged joint density of states (JDOS) $\langle\langle J(\nu)\rangle\rangle$ defined as

$$\langle\langle J(\nu)\rangle\rangle = \int d\nu' \int \frac{d^3\mathbf{k}}{8\pi^3} \text{Tr}[\text{Im}\langle\langle \mathbf{G}(\mathbf{k}, \nu')\rangle\rangle \text{Im}\langle\langle \mathbf{G}(\mathbf{k}, \nu' + \nu)\rangle\rangle]. \quad (32)$$

In other words, $\kappa(\nu, T) \neq |\beta(\nu, T)|J(\nu)$.

Thermal diffusivity captures the effect of disorder in a more striking fashion and gives an idea about the localization. For a harmonic solid, the temperature-independent thermal diffusivity $D(\nu)$ is defined as

$$D(\nu) = \frac{1}{\pi^2}\int d\nu' \int \frac{d^3\mathbf{k}}{8\pi^3} \times \text{Tr}[\text{Im}\mathbf{G}(\mathbf{k}, \nu')\mathbf{S}(\mathbf{k})\text{Im}\mathbf{G}(\mathbf{k}, \nu')\mathbf{S}(\mathbf{k})\text{Im}\mathbf{G}(\mathbf{k}, \nu)] \quad (33)$$

which is similar to the expression of thermal conductivity except that $D(\nu)$ is a product of five random functions instead of four, for a disordered alloy. A similar diagrammatic procedure can be used to calculate the configuration-averaged thermal diffusivity $\langle\langle D(\nu)\rangle\rangle$.

III. NUMERICAL IMPLEMENTATION

I shall now briefly outline the steps of numerical implementation of the developed formalism. As evident from the above section(s), although we have used numerous scattering diagrams to evaluate different contributions to κ, all the contributions are eventually renormalized and expressed in the form of mathematical expressions [e.g., see Eqs. (27), (28), (30), (32), and (33)]. These expressions involve quantities which are essentially related to the atomic masses, dynamical matrices, heat current, and the alloy compositions (x and y). Few of the key quantities involved are the self-energy $\mathbf{\Sigma}$, VCA Green matrix $\mathbf{g}$, configuration-averaged Green matrix $\langle\langle \mathbf{G}\rangle\rangle$, VCA heat-current matrix $\langle\langle \hat{\mathbf{S}}\rangle\rangle$, and effective heat-current matrix $\langle\langle \mathbf{S}_{eff}\rangle\rangle$. I have already shown how to calculate the first three quantities in earlier papers [1,26]. Interested readers are advised to follow these papers for further details. Heat-current matrices involve two-site disorder and hence share exactly the same feature as the dynamical matrices. In fact, they themselves depend on the atomic masses and dynamical matrices [see Eqs. (12) and (13)]. As such, calculation of any quantity involving heat-current matrices can be done in an exactly similar manner as that of dynamical matrices.

I shall now apply the developed formalism on a real binary alloy. It should be noted that the two main quantities which go as an input to our simulation are the atomic masses and the dynamical matrices between respective pairs (A-A, A-B, and B-B pairs for a binary A-xB$_y$ alloy). Atomic masses of different elements are readily available in the literature. The dynamical matrices between different atomic pairs (specially for a random alloy), however, are not trivial to calculate. To demonstrate the strength of the method, I have chosen $Au_{1-x}Fe_x$ alloy as a test case for which a detailed *ab initio* lattice dynamics calculation is done by us recently [27]. One of the main objectives of this paper was to evaluate the dynamical matrices between different pairs within an *ab initio* framework. This was done by combining two complementary techniques, namely, special quasirandom structure (SQS) [28] and the augmented space formalism, which together facilitate a powerful approach to capture the multisite disorder effects, as required in the phonon problem. The simulated nearest-neighbor dynamical matrices between different pairs (Au-Au, Au-Fe, and Fe-Fe) of four different $Au_{1-x}Fe_x$ alloys are listed in Table I of this paper [27]. For further details, readers are referred to Ref. [27]. These force constants along with the atomic masses of the constituent elements ($m_{Au} = 196.97$ amu and $m_{Fe} = 55.85$ amu) are used as the input parameters to our thermal transport simulation, as described below. A similar SQS study of force constants but a different approach to the thermal transport for semiconducting alloys is reported recently [29], where a strong influence of directional bonding is illustrated.

IV. RESULTS AND DISCUSSION

Figure 15 (left) shows the frequency dependence of configuration-averaged lattice thermal conductivity $\langle\langle \kappa(\nu)\rangle\rangle$ and the scaled joint density of states $\langle\langle J(\nu)\rangle\rangle$ at $T = 280$ K for $Au_{50}Fe_{50}$ alloy. The dotted-dashed (red) line shows the thermal conductivity within the VCA approximation where no higher-order disorder corrections are included, while the solid line (black) shows the data where all the disorder-induced corrections including the vertex corrections are explicitly taken into account. It is clear that the effect of renormalized higher-order corrections is not small in the entire phonon frequency range and hence can not be neglected. Thus, the conventional single-site mean field approximation is not sufficient to capture the multiple-scattering phenomenon associated with the phonon transport. It is also evident from the JDOS plot that $\kappa(\nu, T) \neq |\beta(\nu, T)|J(\nu)$, i.e., the transition rate β is strongly dependent both on initial and final energies of the phonon spectrum. Interestingly, both $\langle\langle \kappa(\nu)\rangle\rangle$ and $\langle\langle J(\nu)\rangle\rangle$ have a sharp dip at an extremely small energy ($\nu \to 0$), reflecting the missing intraband (κ^{II}) contribution to the conductivity. Such dip arises due to a smooth convolution of two Green matrices $\mathbf{G}(k, \nu' + \nu)$ and $\mathbf{G}(k, \nu')$. An estimate of the dc thermal conductivity can be obtained by extrapolating our $\langle\langle \kappa(\nu)\rangle\rangle$ curve from a value just above $\nu = 0$ to a value at $\nu = 0$.

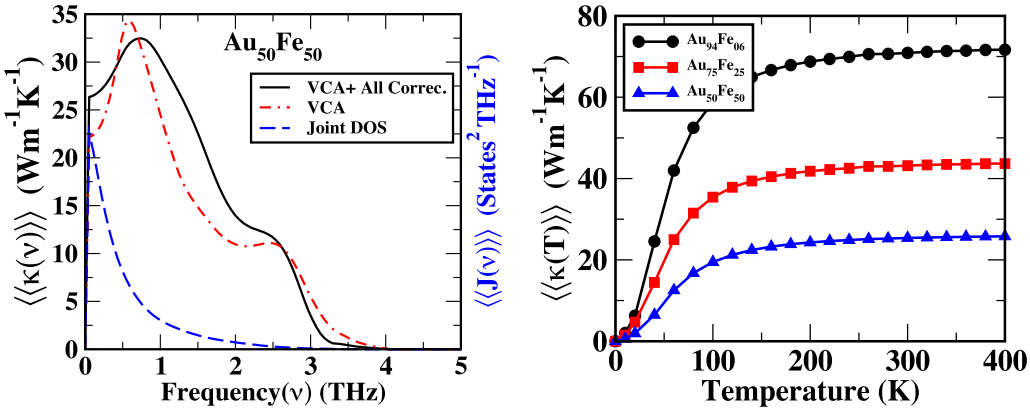

FIG. 15. (Left) Frequency (ν) dependence of configuration-averaged thermal conductivity and joint density of states for $Au_{50}Fe_{50}$ alloy at $T = 280$ K. Solid (black) line shows the result including all disorder-induced corrections + the vertex correction [see Eq. (31)], dotted-dashed (red) line includes the VCA average only, while dashed (blue) line shows the JDOS. (Right) Temperature dependence of $\langle\langle\kappa(T)\rangle\rangle$ for $Au_{94}Fe_{06}$, $Au_{75}Fe_{25}$, and $Au_{50}Fe_{50}$ alloys.

This estimate turns out to be 26.3 W m^{-1} K^{-1} for $Au_{50}Fe_{50}$ alloy. A detailed literature survey shows the availability of only limited experimental data on few dilute binary alloys involving Au. The typical values of the experimental lattice thermal conductivity for pure Au and some of its dilute alloys fall in the range 20–60 W m^{-1} K^{-1} [30]. The right panel of Fig. 15 shows the temperature dependence of $\langle\langle\kappa(T)\rangle\rangle$ for three different $Au_{1-x}Fe_x$ alloys. A close inspection of low T ($T \leqslant 30$ K) behavior of $\kappa(T)$ confirms a quadratic dependence on T, which mainly originates from low-energy vibrations. With further increase in T, $\kappa(T)$ increases and finally saturates to an almost constant value beyond a certain temperature. Such saturation, within harmonic approximation, arises mainly from the T dependence of the Einstein specific-heat part of the κ expression. One can also relate such saturation to the dominant phonon-phonon scattering in the high-T range which becomes so strong that the phonon mean-free path (MFP) reaches a minima. This, in turn, freezes further reduction in MFP due to any enhancement in disorder scattering by raising T and hence resulting in a T-independent κ. Another important observation is the reduction in κ with increasing the disorder concentration (x). This is the most common effect which arises due to the enhanced scattering caused by the difference in atomic masses, radii, and dynamical matrices of the two constituent elements of the alloy. In the present case of Au-Fe alloy, this scattering is dominated mainly by the difference in atomic masses ($M_{Au}/M_{Fe} = 3.53$) because the radii and force constants for Au and Fe are mostly similar.

Thermal diffusivity for alloys is an important descriptor to evaluate the effect of disorder scattering on vibrational states and hence the localization and delocalization of phonon modes. Figure 16 shows the frequency dependence of configuration-averaged thermal diffusivity $\langle\langle D(\nu)\rangle\rangle$ (top) and phonon density of states (bottom) for $Au_{50}Fe_{50}$ alloys. A close look at the high-frequency data indicates that diffusivity decreases smoothly (almost linear in ν) above 4 THz and vanishes (up to the sixth decimal place) at $\nu_c = 5.52$ THz. This critical frequency (ν_c) is called the mobility edge above which the diffusivity strictly goes to zero in the infinite-size limit. I have fitted the diffusivity data in this ν range (4–5.52 THz) with the expression $\langle\langle D(\nu)\rangle\rangle \simeq (\nu_c - \nu)^\alpha$, and found the critical exponent α to be 1.018, which is in fair agreement with the scaling and other theories of Andersen localization [31,32] The allowed vibrational states above (below) the critical frequency give an estimate of the percentage of localized (delocalized) states, as shown by the arrow in the DOS plot. The inset of top panel of Fig. 16 shows the location of mobility edge (ν_c) and the fraction of delocalized states with varying Fe

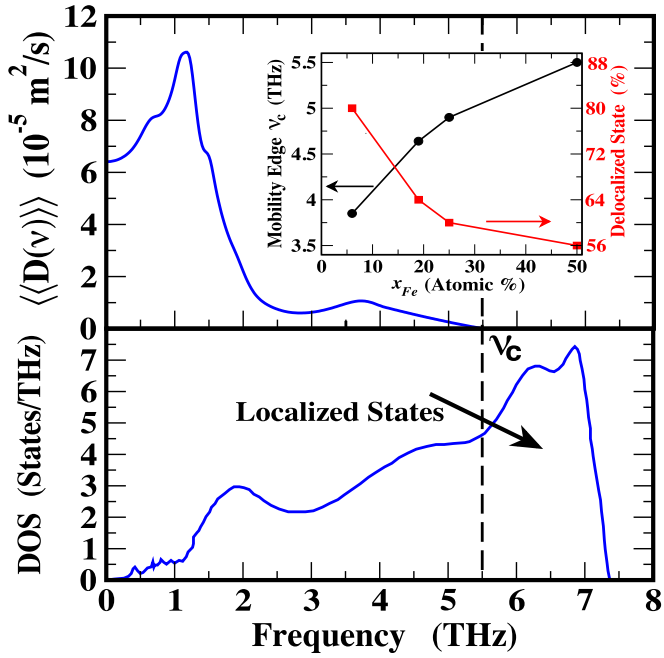

FIG. 16. Configuration-averaged thermal diffusivity $\langle\langle D(\nu)\rangle\rangle$ (top) and phonon density of states, DOS (bottom) vs phonon frequency for $Au_{50}Fe_{50}$ alloy. ν_c locates the mobility edge above which diffusivity goes to zero. The area under the DOS curve above (below) ν_c provide an estimate of the fraction of localized (delocalized) state. The inset in the top panel displays the concentration (x) dependence of the mobility edge and delocalized state for $Au_{1-x}Fe_x$ alloys.

concentration in $Au_{1-x}Fe_x$ alloy. It shows maximum localization at $x_{Fe} = 50$.

V. CONCLUSIONS

I present a generalized multiple-scattering formalism to calculate the configuration-averaged lattice thermal conductivity for random binary alloys. This formulation is based on a conjugation between augmented space method and a Feynman diagrammatic technique. Unlike the single-site-based earlier approaches, the present generalized formulation accurately captures the effect of essential off-diagonal disorder arising out of the dynamical matrices in the phonon problem. I have shown that the effect of disorder scattering can simply be captured by renormalizing the phonon Green functions, via a Dyson equation. Disorder scattering also renormalizes the heat currents. I have explicitly drawn all possible disorder-induced scattering diagrams for single particle as well as two-particle Green functions. The latter corresponds to the lattice thermal conductivity. Apart from the conventional mean-field averaged term in the two-particle Green function expression, there are two relatively dominant classes of correction terms: one which is related to the self-energy and another related to the vertex corrections. I used the Kubo-Greenwood–type formula to first derive the key equations for the lattice thermal transport and then use the augmented space recursion algorithm [20] to obtain the self-energy and the heat-current corrections from it. The expression for the current-current correlation related to the vertex corrections is also derived explicitly.

A similar configuration-averaged scheme is employed to calculate other relevant properties such as joint density of states, thermal diffusion, etc. $Au_{1-x}Fe_x$ binary alloy is then chosen as a test system to apply the presently developed formalism. As compared to the single-site virtual crystal approximation, the disorder-induced higher-order corrections to thermal conductivity ($\langle\langle\kappa\rangle\rangle$) are found to be significant for $Au_{50}Fe_{50}$ alloy. This clearly confirms the strength of the present method. In the low-temperature (T) regime, $\langle\langle\kappa(T)\rangle\rangle$ behaves quadratically, which increases smoothly with increasing T and finally saturates to a constant value at high T. Within harmonic approximation, such saturation in $\kappa(T)$ arises mainly from the T dependence of the Einstein specific-heat part of the κ expression. Configuration-average thermal diffusivity ($\langle\langle D(\nu)\rangle\rangle$) is an important descriptor to evaluate the fraction of localized states. The simulated $\langle\langle D(\nu)\rangle\rangle$ is used to first locate the mobility edge, which is a critical frequency (ν_c) above which the diffusivity is strictly zero in the infinite-size limit. This mobility edge is then used to estimate the % of localized states. I found $Au_{50}Fe_{50}$ alloy to show the maximum localization ($\simeq$44%). In the high-frequency range ($4.0 \leqslant \nu \leqslant 5.52$ eV), $D(\nu)$ is found to decrease smoothly (almost linearly), which when fitted to $D(\nu) \propto (\nu_c - \nu)^{\alpha}$ gives the critical exponent (α) to be 1.018 for $Au_{50}Fe_{50}$ alloy. This agrees fairly well with the scaling and other theories of Andersen localization.

ACKNOWLEDGMENT

I thank the late Abhijit Mookerjee for helping me learn this Feyman diagram technique. I acknowledge DST-SERB (Grant No. MTR/2019/000544) for funding to support this research.

APPENDIX: MATHEMATICAL EXPRESSION FOR DIFFERENT CATEGORIES OF VERTEX CORRECTIONS

This Appendix contains auxiliary elaborations on the mathematical expressions corresponding to seven categories (A–G, see Fig. 13) of ladder scattering diagrams belonging to the vertex corrections.

Category A:

$$\left(W^{\gamma\delta}_{\alpha\beta}\right)_A = (z_1 z_2)^2\, F_\alpha F_\gamma\, \delta_{\alpha\beta}\delta_{\gamma\delta} + 2\, z_2^2\, D^{(2)}_{\alpha\beta}\, F^\gamma\, \delta_{\gamma\delta}.$$

Category B:

$$\begin{aligned}\left(W^{\gamma\delta}_{\alpha\beta}\right)_B = {} & (z_1{}^2 z_2)^2 \left[\sum_{\nu'\nu''} (F_{\alpha\nu'}\delta_{\alpha\nu'})\, G_{R\nu',R\nu''}\, (F_{\nu''\beta}\delta_{\nu''\beta})\right](B_{\nu\delta}\delta_{\nu\delta}) + \left(z_1{}^2 B_{\alpha\beta}\delta_{\alpha\beta}\right)\left(z_2{}^2 B_{\nu\delta}\delta_{\nu\delta}\right) + 2\left[D^{(1)}_{\alpha\beta}\left(z_2{}^2 B_{\nu\delta}\delta_{\nu\delta}\right)\right] \\ & + 4\left[\sum_{\nu'\nu''} D^{(2)}_{\alpha\nu'} G_{R\nu',R\nu''} D^{(2)}_{\nu''\beta}\right](z_2{}^2 B_{\nu\delta}\delta_{\nu\delta}) + 2\left[\sum_{\nu'\nu''} \left(z_1{}^2 F_{\alpha\nu'}\delta_{\alpha\nu'}\right) G_{R\nu',R\nu''} D^{(2)}_{\nu''\beta}\right]\left(z_2{}^2 B_{\nu\delta}\delta_{\nu\delta}\right) + D^{(5)}_{\alpha\beta}\left(z_2{}^2 B_{\nu\delta}\delta_{\nu\delta}\right).\end{aligned}$$

Category C:

$$\begin{aligned}\left(W^{\gamma\delta}_{\alpha\beta}\right)_C = {} & 2\left[\left(z_1{}^2 B_{\alpha\beta}\delta_{\alpha\beta}\right) D^{(1)}_{\nu\delta}\right] + 2\left[\sum_{\nu'\nu''} \left(z_1{}^2 F_{\alpha\nu'}\delta_{\alpha\nu'}\right)\, G_{R\nu',R\nu''}\, \left(z_1{}^2 F_{\nu''\beta}\delta_{\nu''\beta}\right)\right] D^{(1)}_{\nu\delta} + \, 4\, D^{(1)}_{\alpha\beta}\, D^{(1)}_{\nu\delta} \\ & + 8\left[\sum_{\nu'\nu''} D^{(2)}_{\alpha\nu'}\, G_{R\nu',R\nu''}\, D^{(2)}_{\nu''\beta}\right] D^{(1)}_{\nu\delta} + \, 4\left[\sum_{\nu'\nu''} \left(z_1{}^2 F_{\alpha\nu'}\delta_{\alpha\nu'}\right) G_{R\nu',R\nu''}\, D^{(2)}_{\nu''\beta}\right] D^{(1)}_{\nu\delta} \\ & + 2\left[\sum_{\nu'\nu''} D^{(2)}_{\alpha\nu'}\, G_{R\nu',R\nu''}\, \left(z_1{}^2 F_{\nu''\beta}\delta_{\nu''\beta}\right)\right] D^{(1)}_{\nu\delta}.\end{aligned}$$

Category D:

$$\left(W^{\gamma\delta}_{\alpha\beta}\right)_D = 2\left[\left(z_1{}^2 F_{\alpha\beta}\delta_{\alpha\beta}\right)D^{(2)}_{\nu\delta}\right] + 4\, D^{(2)}_{\alpha\beta}\, D^{(2)}_{\nu\delta}.$$

Category E:

$$\begin{aligned}
\left(W^{\gamma\delta}_{\alpha\beta}\right)_E = {} & 2\left[\sum_{\nu'\nu''}\left(z_1{}^2 B_{\alpha\nu'}\delta_{\alpha\nu'}\right) G_{R\nu',R\nu''}\left(z_1{}^2 B_{\nu''\beta}\delta_{\nu''\beta}\right)\right]D^{(3)}_{\nu\delta} \\
& + 8\left[\sum_{\nu'\nu''}\left(z_1{}^2 B_{\alpha\nu'}\delta_{\alpha\nu'}\right)G_{R\nu',R\nu''}\, D^{(1)}_{\nu''\beta}\right]D^{(3)}_{\nu\delta} + 16\left[\sum_{\nu'\nu''} D^{(1)}_{\alpha\nu'}\, G_{R\nu',R\nu''}\, D^{(1)}_{\nu''\beta}\right]D^{(3)}_{\nu\delta} \\
& + 4\left[\sum_{\nu_1\ldots\nu_6}\left(z_1{}^2 F_{\alpha\nu_1}\delta_{\alpha\nu_1}\right) G_{R\nu_1,R\nu_2}\left(z_1{}^2 F_{\nu_2\nu_3}\delta_{\nu_2\nu_3}\right) G_{R\nu_3,R\nu_4}\left(z_1{}^2 F_{\nu_4\nu_5}\delta_{\nu_4\nu_5}\right)G_{R\nu_5,R\nu_6}\left(z_1{}^2 F_{\nu_6\beta}\delta_{\nu_6\beta}\right)\right]D^{(3)}_{\nu\delta} \\
& + 16\left[\sum_{\nu_1\ldots\nu_6}\left(z_1{}^2 F_{\alpha\nu_1}\delta_{\alpha\nu_1}\right) G_{R\nu_1,R\nu_2}\left(z_1{}^2 F_{\nu_2\nu_3}\delta_{\nu_2\nu_3}\right) G_{R\nu_3,R\nu_4}\, D^{(2)}_{\nu_4\nu_5} G_{R\nu_5,R\nu_6}\, D^{(2)}_{\nu_6\beta}\right]D^{(3)}_{\nu\delta} + 4D^{(3)}_{\alpha\beta}\, D^{(3)}_{\nu\delta} \\
& + 4\left[\sum_{\nu'\nu''}\left(z_1{}^2 F_{\alpha\nu'}\delta_{\alpha\nu'}\right) G_{R\nu',R\nu''}\, D^{(4)}_{\nu''\beta}\right]D^{(3)}_{\nu\delta} + 4\left[\sum_{\nu'\nu''}\left(z_1{}^2 F_{\alpha\nu'}\delta_{\alpha\nu'}\right)G_{R\nu',R\nu''}\, D^{(5)}_{\nu''\beta}\right]D^{(3)}_{\nu\delta} \\
& + 4\left[\sum_{\nu_1\ldots\nu_4}\left(z_1{}^2 B_{\alpha\nu_1}\delta_{\alpha\nu_1}\right) G_{R\nu_1,R\nu_2}\left(z_1{}^2 F_{\nu_2\nu_3}\delta_{\nu_2\nu_3}\right)G_{R\nu_3,R\nu_4}\left(z_1{}^2 F_{\nu_4\delta}\delta_{\nu_4\delta}\right)\right]D^{(3)}_{\nu\delta} \\
& + 16\left[\sum_{\nu_1\ldots\nu_4}\left(z_1{}^2 B_{\alpha\nu_1}\delta_{\alpha\nu_1}\right) G_{R\nu_1,R\nu_2}\left(D^{(2)}_{\nu_2\nu_3}\right)G_{R\nu_3,R\nu_4}\left(D^{(2)}_{\nu_4\beta}\right)\right]D^{(3)}_{\nu\delta} \\
& + 8\left[\sum_{\nu_1\ldots\nu_4}\left(z_1{}^2 F_{\alpha\nu_1}\delta_{\alpha\nu_1}\right) G_{R\nu_1,R\nu_2}\left(z_1{}^2 F_{\nu_2\nu_3}\delta_{\nu_2\nu_3}\right)G_{R\nu_3,R\nu_4}\left(D^{(1)}_{\nu_4\beta}\right)\right]D^{(3)}_{\nu\delta} \\
& + 4\left[\sum_{\nu_1\ldots\nu_4}\left(z_1{}^2 F_{\alpha\nu_1}\delta_{\alpha\nu_1}\right) G_{R\nu_1,R\nu_2}\left(z_1{}^2 F_{\nu_2\nu_3}\delta_{\nu_2\nu_3}\right)G_{R\nu_3,R\nu_4}\left(D^{(5)}_{\nu_4\beta}\right)\right]D^{(3)}_{\nu\delta} \\
& + 32\left[\sum_{\nu_1\ldots\nu_4}\left(D^{(1)}_{\alpha\nu_1}\right) G_{R\nu_1,R\nu_2}\left(D^{(2)}_{\nu_2\nu_3}\right)G_{R\nu_3,R\nu_4}\left(D^{(2)}_{\nu_4\beta}\right)\right]D^{(3)}_{\nu\delta} \\
& + 16\left[\sum_{\nu_1\ldots\nu_4}\left(D^{(2)}_{\alpha\nu_1}\right) G_{R\nu_1,R\nu_2}\left(D^{(2)}_{\nu_2\nu_3}\right)G_{R\nu_3,R\nu_4}\left(D^{(5)}_{\nu_4\beta}\right)\right]D^{(3)}_{\nu\delta} + 5\left[\sum_{\nu'\nu''}\left(D^{(5)}_{\alpha\nu'}\right) G_{R\nu',R\nu''}\left(D^{(5)}_{\nu''\beta}\right)\right]D^{(3)}_{\nu\delta} \\
& + 64\left[\sum_{\nu_1\ldots\nu_6}\left(D^{(2)}_{\alpha\nu_1}\right) G_{R\nu_1,R\nu_2}\left(D^{(2)}_{\nu_2\nu_3}\right)G_{R\nu_3,R\nu_4}\left(D^{(2)}_{\nu_4\nu_5}\right)G_{R\nu_5,R\nu_6}\left(D^{(2)}_{\nu_6\beta}\right)\right]D^{(3)}_{\nu\delta}.
\end{aligned}$$

Category F:

$$\begin{aligned}
\left(W^{\gamma\delta}_{\alpha\beta}\right)_F = {} & 6\left[\sum_{\nu'\nu''}\left(z_1{}^2 B_{\alpha\nu'}\delta_{\alpha\nu'}\right) G_{R\nu',R\nu''}\left(z_1{}^2 F_{\nu''\beta}\delta_{\nu''\beta}\right)\right]D^{(4)}_{\nu\delta} + 12\left[\sum_{\nu'\nu''}\left(D^{(1)}_{\alpha\nu'}\right)G_{R\nu',R\nu''}\left(z_1{}^2 F_{\nu''\beta}\delta_{\nu''\beta}\right)\right]D^{(4)}_{\nu\delta} \\
& + 24\left[\sum_{\nu'\nu''}\left(D^{(1)}_{\alpha\nu'}\right) G_{R\nu',R\nu''}\left(D^{(2)}_{\nu''\beta}\right)\right]D^{(4)}_{\nu\delta} + 12\left[\sum_{\nu'\nu''}\left(z_1{}^2 B_{\alpha\nu'}\delta_{\alpha\nu'}\right) G_{R\nu',R\nu''}\left(D^{(2)}_{\nu''\beta}\right)\right]D^{(4)}_{\nu\delta} + 12\, D^{(4)}_{\alpha\beta}\, D^{(4)}_{\nu\delta} \\
& + 10\left[\sum_{\nu'\nu''}\left(D^{(5)}_{\alpha\nu'}\right) G_{R\nu',R\nu''}\left(z_1{}^2 F_{\nu''\beta}\delta_{\nu''\beta}\right)\right]D^{(4)}_{\nu\delta} + 20\left[\sum_{\nu'\nu''}\left(D^{(5)}_{\alpha\nu'}\right) G_{R\nu',R\nu''}\left(D^{(2)}_{\nu''\beta}\right)\right]D^{(4)}_{\nu\delta} \\
& + 10\left[\sum_{\nu'\nu''}\left(z_1{}^2 F_{\alpha\nu'}\delta_{\alpha\nu'}\right) G_{R\nu',R\nu''}\left(D^{(5)}_{\nu''\beta}\right)\right]D^{(4)}_{\nu\delta} + 20\left[\sum_{\nu'\nu''}\left(D^{(2)}_{\alpha\nu'}\right) G_{R\nu',R\nu''}\left(D^{(5)}_{\nu''\beta}\right)\right]D^{(4)}_{\nu\delta}.
\end{aligned}$$

Category G:

$$\left(W^{\gamma\delta}_{\alpha\beta}\right)_G = \left(z_1{}^2 B_{\alpha\beta}\delta_{\alpha\beta}\right) D^{(5)}_{\nu\delta} + 2D^{(1)}_{\alpha\beta}D^{(5)}_{\nu\delta} + 4D^{(5)}_{\alpha\beta}D^{(5)}_{\nu\delta} + 4\left[\sum_{\nu'\nu''}\left(z_1{}^2 F_{\alpha\nu'}\delta_{\alpha\nu'}\right) G_{R\nu',R\nu''}\left(z_1{}^2 F_{\nu''\beta}\delta_{\nu''\beta}\right)\right] D^{(5)}_{\nu\delta}$$
$$+ 8\left[\sum_{\nu'\nu''}\left(z_1{}^2 F_{\alpha\nu'}\delta_{\alpha\nu'}\right) G_{R\nu',R\nu''}\left(D^{(2)}_{\nu''\beta}\right)\right] D^{(5)}_{\nu\delta} + 8\left[\sum_{\nu'\nu''}\left(D^{(2)}_{\alpha\nu'}\right) G_{R\nu',R\nu''}\left(z_1{}^2 F_{\nu''\beta}\,\delta_{\nu''\beta}\right)\right] D^{(5)}_{\nu\delta}$$
$$+ 16\left[\sum_{\nu'\nu''}\left(D^{(2)}_{\alpha\nu'}\right) G_{R\nu',R\nu''}\left(D^{(2)}_{\nu''\beta}\right)\right] D^{(5)}_{\nu\delta}.$$

[1] A. Alam and A. Mookerjee, Phys. Rev. B **69**, 024205 (2004).
[2] Y. Tsunoda, N. Kunitomi, N. Wakabayashi, R. M. Nicklow, and H. G. Smith, Phys. Rev. B **19**, 2876 (1979).
[3] P. L. Leath, Phys. Rev. B **2**, 3078 (1970).
[4] J. K. Flicker and P. L. Leath, Phys. Rev. B **7**, 2296 (1973).
[5] D. W. Taylor, Phys. Rev. **156**, 1017 (1967).
[6] H. Shiba, Prog. Theor. Phys. **40**, 435 (1968); G. Grunewald, J. Phys. F: Met. Phys. **6**, 999 (1976); T. Kaplan and M. Mostoller, Phys. Rev. B **9**, 353 (1974); R. Mills and P. Ratanavararaksa, *ibid.* **18**, 5291 (1978); T. Kaplan, P. L. Leath, L. J. Gray, and H. W. Diehl, *ibid.* **21**, 4230 (1980).
[7] M. Yussouff and A. Mookerjee, J. Phys. C: Solid State Phys. **17**, 1009 (1984); A. Mookerjee and R. P. Singh, *ibid.* **18**, 4261 (1985); J. Phys. F: Met. Phys. **18**, 2171 (1988).
[8] T. Kaplan and L. J. Gray, Phys. Rev. B **14**, 3462 (1976); L. J. Gray and T. Kaplan, *ibid.* **24**, 1872 (1981).
[9] D. A. Rowlands, J. B. Staunton, B. L. Gyorffy, E. Bruno, and B. Ginatempo, Phys. Rev. B **72**, 045101 (2005); D. A. Biava, S. Ghosh, D. D. Johnson, W. A. Shelton, and A. V. Smirnov, *ibid.* **72**, 113105 (2005).
[10] M. Jarrell and H. R. Krishnamurthy, Phys. Rev. B **63**, 125102 (2001)
[11] S. Ghosh, P. L. Leath, and Morrel H. Cohen, Phys. Rev. B **66**, 214206 (2002)
[12] C. E. Ekuma, H. Terletska, K.-M. Tam, Z.-Y. Meng, J. Moreno, and M. Jarrell, Phys. Rev. B **89**, 081107(R) (2014).
[13] A. Weiße and H. Fehske, *Computational Many-Particle Physics*, Lecture Notes in Physics (Springer, Berlin, 2008), Vol. 739, pp. 529–544.
[14] P. Markos, Acta Phys. Slovaca **56**, 561 (2006).
[15] A. Weiße, G. Wellein, A. Alvermann, and H. Fehske, Rev. Mod. Phys. **78**, 275 (2006).
[16] A. Mookerjee, J. Phys. C: Solid State Phys. **6**, L205 (1973).
[17] T. Saha, I. Dasgupta and A. Mookerjee, J. Phys.: Condens. Matter **6**, L245 (1994).
[18] A. Mookerjee and R. Prasad, Phys. Rev. B **48**, 17724 (1993).
[19] A. Alam, R. K. Chouhan and A. Mookerjee, Phys. Rev. B **83**, 054201 (2011).
[20] A. Alam and A. Mookerjee, Phys. Rev. B **72**, 214207 (2005).
[21] A. Mookerjee, in *Electronic Structure of Alloys, Surfaces and Clusters*, edited by D. D. Sarma and A. Mookerjee (Taylor and Francis, London, 2003).
[22] S. Ghosh, N. Dash, and A. Mookerjee, Mod. Phys. Lett. B **13**, 723 (1999).
[23] R. J. Hardy, Phys. Rev. **132**, 168 (1963).
[24] P. B. Allen and J. L. Feldman, Phys. Rev. B **48**, 12581 (1993).
[25] K. K. Saha and A. Mookerjee, Phys. Rev. B **70**, 134205 (2004).
[26] A. Alam, S. Ghosh, and A. Mookerjee, Phys. Rev. B **75**, 134202 (2007).
[27] J. Kangsabanik, R. K. Chouhan, D. D. Johnson, and A. Alam, Phys. Rev. B **96**, 100201(R) (2017).
[28] A. Zunger, S.-H. Wei, L. G. Ferreira, and J. E. Bernard, Phys. Rev. Lett. **65**, 353 (1990).
[29] M. Arrigoni, J. Carrete, N. Mingo, and G. K. H. Madsen, Phys. Rev. B **98**, 115205 (2018).
[30] G. K. White, S. B. Woods, and M. T. Elford, Philos. Mag. **4**, 688 (1959); R. S. Crisp and J. Rungis, *ibid.* **22**, 217 (1970).
[31] P. W. Andersen, Phys. Rev. **109**, 1492 (1958).
[32] P. A. Lee and T. V. Ramakrishnan, Rev. Mod. Phys. **57**, 287 (1985).